# Band structures in ^{101}Pd

V. Singh, S. Sihotra, G. H. Bhat, J. A. Sheikh, M. Kaur, S. Kumar, K. Singh, J. Goswamy, S. Saha, J. Sethi, R. Palit, S. S. Malik, N. Singh, U. Garg, and D. Mehta

Phys. Rev. C **95**, 064312 — Published 14 June 2017

DOI: 10.1103/PhysRevC.95.064312

# Band structures in $^{101}$Pd

V. Singh[1], S. Sihotra[1],* G. H. Bhat[2,3], J. A. Sheikh[2], M. Kaur[1], S. Kumar[1], K. Singh[1], J. Goswamy[1], S. Saha[4], J. Sethi[4],† R. Palit[4], S. S. Malik[5], N. Singh[1], U. Garg[6], and D. Mehta[1]

[1]*Department of Physics, Panjab University, Chandigarh-160014, India*
[2]*Department of Physics, University of Kashmir, Srinagar-190006, India*
[3]*Department of Physics, Govt. Degree College Kulgam-192231, India*
[4]*Department of Nuclear and Atomic Physics, TIFR, Mumbai-400005, India*
[5]*Department of Physics, Guru Nanak Dev University, Amritsar-143005, India and*
[6]*Department of Physics, University of Notre Dame, Notre Dame, Indiana 46556*

(Dated: May 21, 2017)

Excited states in the $^{101}$Pd nucleus were investigated through the $^{75}$As($^{31}$P, $2p3n$) fusion-evaporation reaction at $E_{lab}$= 125 MeV using the Indian National Gamma Array (INGA) spectrometer equipped with 21 clover Ge detectors. The level scheme is considerably extended for medium spin values. New positive-parity band structures in $^{101}$Pd have been studied within the framework of the projected shell model (PSM) and are found to undergo transition from single quasiparticle to high-K three quasiparticle configuration after bandcrossing, i.e., from principal-axis rotation to tilted-axis rotation. The negative-parity band structures are discussed in the framework of the hybrid version of tilted-axis cranking (TAC) shell model calculations. The observed alignment gain in the lowest excited $\nu h_{11/2}$ negative-parity band results from successive $(\nu g_{7/2})^2$ and $(\pi g_{9/2})^2$ pair alignments. The higher excited negative-parity bands are reproduced for the $\nu[h_{11/2}(g_{7/2}/d_{5/2})^2]$ and $(\pi g_{9/2})^{-2} \otimes \nu h_{11/2}$ configurations.

**PACS numbers:** [21.10.-k, 21.60.-n, 23.20.-g, 27.60.+j]

## I. INTRODUCTION

In the neutron-deficient nuclei approaching the neutron and proton major shell closures at N = Z = 50, the experimental and theoretical investigations have revealed diversity in band structures resulting from coupling of the valence nucleons with different shape-driving effects and the core-excited configurations [1]. Various new phenomena have been identified, viz., smooth band termination (ST), magnetic rotation (MR) and antimagnetic rotation (AMR), wherein angular momentum is generated through gradual alignment of the valence proton hole and the neutron particle angular momenta with different initial geometrical compositions [2]. These exhibit band structures with different magnitude and trends of the dynamic moment of inertia, and the transition rates as a function of angular momentum. Band structures in the $^{98-100}$Ru [3], $^{101-102}$Rh [4,5], $^{98-100,102,103}$Pd [6–10], and $^{98,99}$Ag [11,12] isotopes have been observed up to termination and interpreted as the valence-space and the particle-hole core-excited configurations. Magnetic rotation bands with configurations involving proton holes from the $g_{9/2}$ orbital and neutron particles from the $h_{11/2}$ and $g_{7/2}$ or $d_{5/2}$ orbitals have been reported in $^{103-107}$Ag [13], $^{108-110}$Cd [14], $^{108,110}$In [15], and $^{105,106,108}$Sn [16]. In such bands, the magnetic rotor assimilate closing of the blades of a pair of shears involving angular momenta of proton holes and neutron particles. The AMR bands based on the $\pi g_{9/2}^{-2}$ related configurations have been identified in $^{105-108,110}$Cd [17,18] and $^{104}$Pd [19] on the basis of lifetime measurements. These bands are generated by simultaneous closing of a pair of $g_{9/2}^{-1}$ proton angular momentum blades towards the neutron angular momentum in the twin shears geometry. The observed slower fall of $B(E2)$ values in $^{110}$Cd as compared to those observed in pure AMR bands in the $^{106,108}$Cd isotopes evidence interplay between antimagnetic and core rotation [18]. In $^{102}$Pd [20], exceptionally long vibrational band has also been reported which exhibits sharp increasing trend of the B(E2) values with spin, and is indicative of angular momentum generation by increasing deformation. It is explained as tidal wave travelling over the nuclear surface with constant angular velocity.

The present work focuses on new experimental data obtained for the excited states of $^{101}$Pd using an advanced array of Compton-suppressed clover detectors. Prior to this work, high spin states in this nucleus have previously been investigated by Zhou *et al.* [21] and Sugawara *et al.* [22] via the $^{76}$Ge($^{28}$Si, $3n$) and $^{68}$Zn($^{37}$Cl, $p3n$) reactions, respectively, and using small arrays of Ge detectors with BGO anti-Compton shields. The quasirotational bands built on the $\nu d_{5/2}$, $\nu g_{7/2}$, and $\nu h_{11/2}$ orbitals, and the related configurations have been reported in $^{101}$Pd. Sugawara *et al.* have reported the lifetime measurements in the $\nu h_{11/2}$ band and the observed decreasing trend of the B(E2) rates has been interpreted as antimagnetic rotation (AMR) [23,24]. The present work reports the extended level scheme of $^{101}$Pd nucleus investigated using a high efficiency Compton-suppressed array. The positive-parity and negative-parity band structures are interpreted in the framework of projected shell model (PSM) calculations and tilted-axis cranking (TAC) shell model calculations, respectively.

* Corresponding author: ssihotra@pu.ac.in
† Present address: Department of Chemistry and Biochemistry, University of Maryland, College Park, MD 20742, USA

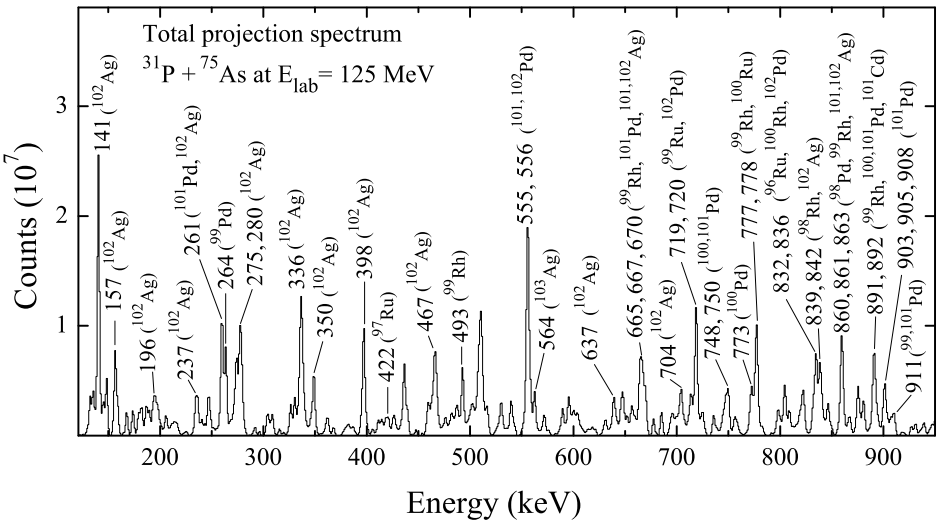


FIG. 1. Total projection spectrum of $E_\gamma$-$E_\gamma$ matrix showing the prominent $\gamma$ rays of various nuclei populated in the present experiment.

## II. EXPERIMENTAL DETAILS

Excited states in the $^{101}$Pd nucleus were populated in the $^{75}$As($^{31}$P, $2p3n$) fusion-evaporation reaction at $E_{lab}$ = 125 MeV. The deexcitations were investigated through in-beam $\gamma$ ray spectroscopic techniques. The $^{31}$P beam was provided by the Pelletron-LINAC facility at TIFR, Mumbai. The $^{75}$As target of thickness 2.8 mg cm$^{-2}$ was prepared by vacuum evaporation and rolled onto a 10 mg cm$^{-2}$ thick Pb backing. The $^{106}$Cd compound nucleus produced in the present reaction is found to decay via several reaction channels associated with the (i) 5-particle emission, viz., $2p3n$ ($^{101}$Pd), $\alpha p3n$ ($^{98}$Rh), and $p4n$ ($^{101}$Ag) with relative population of $\sim$ 8%, 4%, and 13%, respectively, (ii) 4-particle emission, viz., $\alpha p2n$ ($^{99}$Rh), $\alpha 3n$ ($^{99}$Pd), $p3n$ ($^{102}$Ag), and $2p2n$ ($^{102}$Pd) with relative population of $\sim$ 14%, 6%, 5%, and 16%, respectively, and (iii) 3-particle emission, viz. $\alpha 2n$ ($^{100}$Pd) and $p2n$ ($^{103}$Ag) with relative population of $\sim$ 4% and 5%, respectively. Total projection spectrum of $E_\gamma - E_\gamma$ matrix showing the prominent $\gamma$ rays of various populated nuclei is shown in Fig. 1. The deexciting $\gamma$ rays were detected using the Indian National Gamma Array (INGA) comprising 21 Compton suppressed clover detectors [25,26]. With the full assemblage of 24 clover detectors, the photopeak efficiency of INGA is $\sim$ 5% at the 1.3 MeV $\gamma$ ray energy. The clover detectors used in the addback mode resulted in enhanced efficiency for the high energy $\gamma$ rays above $\sim$ 1 MeV. The efficiency of the array for energies up to $\sim$ 3 MeV were deduced from the measured $\gamma$ ray spectra of the $^{133}$Ba and $^{152}$Eu standard radioactive sources and the intensity balance along the transition sequence in higher-lying transition gated coincidence spectra in the $^{38}$Ar, $^{39}$K, and $^{96}$Ru nuclei populated in the present experiment. The details are given elsewhere [27,28].

Two and higher fold clover coincidence events were recorded in a fast digital data aquisition system based on Pixie-16 modules of XIA LLC [25]. The data sorting routine "multi parameter time stamped based coincidence search program (MARCOS)" developed at TIFR [25] was used to sort the time stamped data to generate $E_\gamma$-$E_\gamma$ matrices and $E_\gamma$-$E_\gamma$-$E_\gamma$ cubes compatible with RADWARE format [29]. There were 3.2x10$^8$ events in cube which were analysed by using the RADWARE program LEVIT8R [29] to develop the level scheme. Table I lists all the $\gamma$ rays assigned to $^{101}$Pd along with their intensities and proposed placements in the present level scheme.

For the INGA geometry, the expected value of the DCO ratio is typically $\geq$1.0 for the quadrupole transition and $\leq$0.6 for the dipole transition with gate on the stretched $E2$ transition. However, DCO ratio values $\sim$1 are also expected for pure $\Delta I$ = 0 dipole transitions [3]. To determine the electric or magnetic nature of the $\gamma$ rays, the measurements were performed using the clover detectors at 90° as Compton polarimeter. The integrated polarization directional correlation from oriented nuclei (IPDCO) analysis [30] was performed using two asymmetric polarization matrices corresponding to the parallel and perpendicular segments (with respect to the emission plane) of the clover detector chosen as a Compton polarimeter along one axis and the coincident $\gamma$ rays in all the detectors along the other axis. The DCO and IPDCO ratio values along with the assigned multipolarities for various transitions are also included in Table I.

## III. RESULTS

The ground state of $^{101}$Pd is $I^\pi = 5/2^+$ with $T_{1/2}$ = 8.47 h [31]. Detailed spectroscopic investigations of low-lying states in $^{101}$Pd populated through the $\beta^+$ and EC radioactive decay of $^{101}$Ag [31,32] have led to identification of first isomeric excited $3/2^+$ state at 80.3 keV with a half-life of

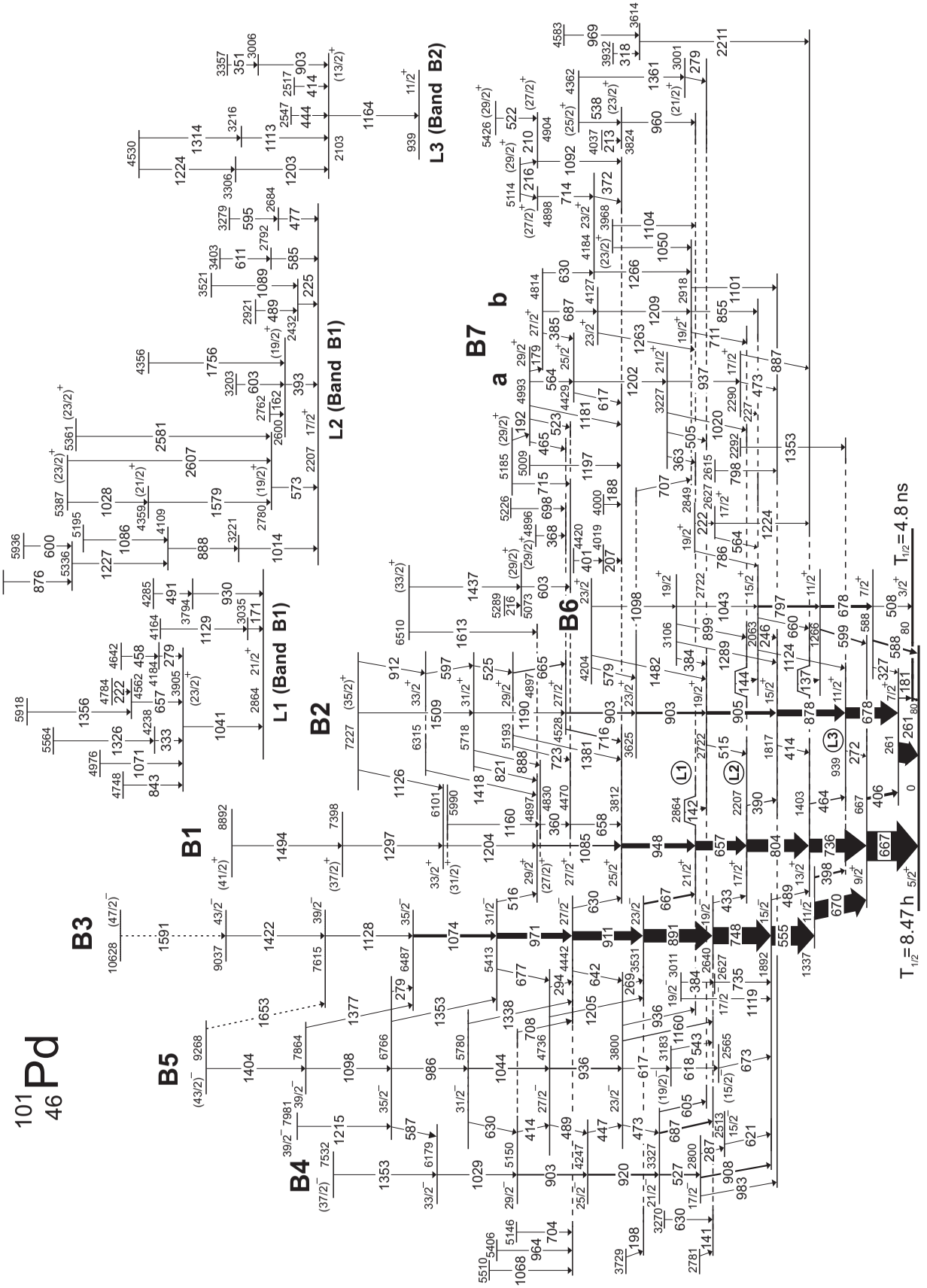


FIG. 2. Level scheme of $^{101}$Pd obtained from the present work. Energies of $\gamma$ rays and levels are given in keV. The width of the arrows is proportional to the relative $\gamma$ ray intensity. The level strucutres built on levels labeled L1, L2, and L3 of bands B1 and B2 are shown separately.

4.8 (5) ns. The present level scheme of $^{101}$Pd (Fig. 2) consists of positive-parity bands B1, B2, B6, and B7, and negative-parity bands B3, B4, and B5. The earlier reported level schemes [21,22,33,34] are modified and extended significantly at medium spins with addition of more than 100 new $\gamma$ transitions. Because of larger fraction of the higher-fold $\gamma$ ray coincidence events collected using INGA and enhanced efficiency using clover detectors in the add-back mode, a large number of weak $\gamma$ transitions could be placed in the level scheme. The sensivity achieved by "double-gating" and the presence of many crossover transitions and interband transitions in the level scheme provide many checks on the placement and ordering of transitions and serve to augment confidence in the correctness of the proposed level scheme. A number of new levels in the present level scheme also result from the coupled structures feeding the levels of either the positive-parity bands or the negative-parity bands.

The $\gamma$ ray transition energies in general agree within $\sim$ 1 keV with those given by Sugawara *et al.* [22] with the few exceptions, e.g., the 516.3 keV ($31/2^- \rightarrow 29/2^+$), 621.2 keV ($15/2^- \rightarrow 15/2^+$), 666.8 keV ($23/2^- \rightarrow 21/2^+$), where the earlier reported level scheme [22] lacks support of transition energy sums. It may be added that many transitions in the level scheme of $^{101}$Pd have energies close-lying to those of transitions in the other populated nuclei, viz., $^{99}$Rh [27], $^{100,102}$Pd [8,9,35], and $^{102}$Ag [28]. The present values deduced from high statistics data using double gated spectra are more reliable. The results related to the positive-parity and the negative-parity bands are discussed in the following sections.

TABLE I: The energies ($E_\gamma$), deexciting (exciting) level energies $E_{i(f)}$, relative intensities ($I_\gamma$), spin-parity assignments ($I_i^\pi \rightarrow I_f^\pi$), DCO and IPDCO ratios, and multipolarity assignments for the $\gamma$ transitions in $^{101}$Pd. In the second column, the $E_i$ values are given unless placed in parentheses which correspond to $E_f$ values for $\gamma$ rays that are not shown in the level scheme. The level structures L1, L2, and L3 are also mentioned alongwith $E_i$. The DCO ratios are obtained from the gated spectra on the stretched E2 transitions as mentioned in the text. The uncertainty in energies of intense $\gamma$ rays is 0.3 keV. It increases up to 1.0 keV for the weak high energy $\gamma$ rays.

| $E_\gamma$(keV) | $E_{i(f)}$(keV) | Intensity ($I_\gamma$) | Spin assignment ($I_i^\pi \rightarrow I_f^\pi$) | DCO | IPDCO | Multipolarity assignment |
|---|---|---|---|---|---|---|
| 80.3 | 80 | 67 (7) | $3/2^+ \rightarrow 5/2^+$ | | | $M1$ |
| 137.2 | 1403 | 40 (5) | $13/2^+ \rightarrow 11/2^+$ | 0.58 (7) | | $M1$ |
| 141.2 | 2781 | $\sim$2 | $\rightarrow 19/2^-$ | | | |
| 142.4 | 2864 | 13 (3) | $21/2^+ \rightarrow 19/2^+$ | | | $M1$ |
| 144.2 | 2207 | 27 (4) | $17/2^+ \rightarrow 15/2^+$ | 0.51 (8) | | $M1$ |
| 161.9 | 2762 (L2) | 7 (2) | $\rightarrow (19/2)^+$ | | | |
| 171.2 | 3035 (L1) | $\sim$2 | $\rightarrow 21/2^+$ | | | |
| 179.1 | 4993 | 4 (1) | $29/2^+ \rightarrow 27/2^+$ | | | $M1$ |
| 180.8 | 261 | 38 (5) | $7/2^+ \rightarrow 3/2^+$ | 0.94 (12) | | $E2$ |
| 186.1 | (4184) | $\sim$1 | $\rightarrow 23/2^+$ | | | |
| 187.9 | 4000 | $\sim$1 | $\rightarrow 25/2^+$ | | | |
| 192.1 | 5185 | 4 (1) | $(29/2)^+ \rightarrow 29/2^+$ | | | |
| 198.1 | 3729 | $\sim$2 | $\rightarrow 23/2^-$ | | | |
| 206.9 | 4019 | $\sim$2 | $\rightarrow 25/2^+$ | | | |
| 210.1 | 5114 | 3 (1) | $(29/2)^+ \rightarrow (27/2)^+$ | | | ($M1$) |
| 212.9 | 4037 | 5 (1) | $\rightarrow (23/2)^+$ | | | |
| 215.9 | 5289 | $\sim$2 | $\rightarrow (29/2)^+$ | | | |
| 216.2 | 5114 | $\sim$2 | $(29/2)^+ \rightarrow (27/2)^+$ | | | ($M1$) |
| 222.1 | 4784 (L2) | $\sim$1 | | | | |
| 222.4 | 2849 | 3 (1) | $19/2^+ \rightarrow 17/2^+$ | | | $M1$ |
| 225.1 | 2432 (L2) | 7 (2) | $\rightarrow 17/2^+$ | | | |
| 226.9 | 2290 | 16 (3) | $17/2^+ \rightarrow 15/2^+$ | 0.64 (10) | | $M1$ |
| 245.8 | 2063 | 25 (4) | $15/2^+ \rightarrow 15/2^+$ | 0.92 (18) | -0.12 (2) | $M1$ |
| 261.0 | 261 | 671 (35) | $7/2^+ \rightarrow 5/2^+$ | | | $M1$ |
| 268.9 | 3800 | 16 (3) | $23/2^- \rightarrow 23/2^-$ | 1.02 (18) | | $M1$ |
| 272.1 | 939 | 28 (5) | $11/2^+ \rightarrow 9/2^+$ | 0.68 (9) | -0.07 (1) | M1 |
| 278.7 | 6766 | 5 (1) | $35/2^- \rightarrow 35/2^-$ | | | |
| 279.0 | 4184 (L1) | $\sim$2 | $\rightarrow (23/2)^+$ | | | |
| 279.2 | 3001 | 5 (1) | $(21/2)^+ \rightarrow 19/2^+$ | | | ($M1$) |
| 286.8 | 2800 | 18 (4) | $17/2^- \rightarrow 15/2^-$ | 0.68 (10) | -0.05 (1) | $M1$ |
| 293.9 | 4736 | 6 (1) | $27/2^- \rightarrow 27/2^-$ | | | |
| 317.9 | 3932 | 4 (1) | | | | |
| 326.8 | 588 | 21 (3) | $7/2^+ \rightarrow 7/2^+$ | 0.89 (16) | -0.04 (1) | $M1$ |
| 332.8 | 4238 (L1) | 5 (1) | $\rightarrow (23/2)^+$ | | | |
| 351.1 | 3357 (L3) | $\sim$1 | | | | |
| 360.0 | 4830 | 5 (1) | $(27/2)^+ \rightarrow 27/2^+$ | | | |
| 363.1 | 3227 | 21 (3) | $21/2^+ \rightarrow 21/2^+$ | 0.88 (16) | -0.07 (2) | $M1$ |
| 368.3 | 4896 | 17 (3) | $(29/2)^+ \rightarrow 27/2^+$ | 0.65 (9) | | ($M1$) |

**TABLE I –(continued)**

| $E_\gamma$(keV) | $E_{i(f)}$(keV) | Intensity | Spin assignment ($I_i^\pi \rightarrow I_f^\pi$) | DCO | IPDCO | Multipolarity assignment |
|---|---|---|---|---|---|---|
| 372.0 | 4184 | 12 (2) | $23/2^+ \rightarrow 25/2^+$ | 0.57 (12) | | $M1$ |
| 384.0 | 3011 | 15 (2) | $19/2^- \rightarrow 17/2^-$ | 0.55 (12) | | $M1$ |
| 384.2 | 3106 | 19 (4) | $19/2^+ \rightarrow 19/2^+$ | 0.91 (11) | -0.10 (2) | $M1$ |
| 385.3 | 4814 | 4 (1) | $27/2^+ \rightarrow 25/2^+$ | | | $M1$ |
| 390.2 | 2207 | 35 (5) | $17/2^+ \rightarrow 15/2^+$ | 0.63(8) | -0.06 (2) | $M1$ |
| 391.9 | (4470) | $\sim$2 | $\rightarrow 25/2^+$ | | | |
| 393.0 | 2600 (L2) | 17 (3) | $(19/2)^+ \rightarrow 17/2^+$ | 0.50 (8) | | ($M1$) |
| 398.2 | 1337 | 65 (6) | $11/2^- \rightarrow 11/2^+$ | 0.88 (12) | 0.04 (1) | $E1$ |
| 401.3 | 4420 | $\sim$1 | | | | |
| 405.9 | 667 | 98 (7) | $9/2^+ \rightarrow 7/2^+$ | 0.48 (6) | -0.04 (1) | $M1$ |
| 413.9 | 5150 | 15 (3) | $29/2^- \rightarrow 27/2^-$ | 0.62 (10) | | $M1$ |
| 414.1 | 1817 | 27 (4) | $15/2^+ \rightarrow 13/2^+$ | 0.56 (10) | -0.04 (1) | $M1$ |
| 414.2 | 2517 (L3) | $\sim$1 | $\rightarrow (13/2)^+$ | | | |
| 432.9 | 2640 | 19 (4) | $19/2^- \rightarrow 17/2^+$ | 0.68 (14) | 0.06 (2) | $E1$ |
| 444.2 | 2547 (L3) | $\sim$2 | $\rightarrow (13/2)^+$ | | | |
| 446.9 | 4247 | 16 (3) | $25/2^- \rightarrow 23/2^-$ | 0.55 (8) | | $M1$ |
| 458.1 | 4642 (L1) | $\sim$1 | | | | |
| 464.3 | 1403 | 39 (5) | $13/2^+ \rightarrow 11/2^+$ | 0.66 (8) | | $M1$ |
| 465.3 | 4993 | 16 (3) | $29/2^+ \rightarrow 27/2^+$ | 0.53 (10) | | $M1$ |
| 473.1 | 2290 | 22 (4) | $17/2^+ \rightarrow 15/2^+$ | 0.68 (14) | -0.13 (3) | $M1$ |
| 473.3 | 3800 | 23 (4) | $23/2^- \rightarrow 21/2^-$ | 0.67 (14) | -0.10 (3) | $M1$ |
| 477.1 | 2684 (L2) | 7 (2) | $\rightarrow 17/2^+$ | | | |
| 488.8 | 2921 (L2) | $\sim$1 | | | | |
| 489.0 | 4736 | 13 (3) | $27/2^- \rightarrow 25/2^-$ | 0.65 (18) | | $M1$ |
| 489.1 | 1892 | 29 (5) | $15/2^- \rightarrow 13/2^+$ | 0.57 (9) | 0.08 (2) | $E1$ |
| 491.3 | 4285 (L1) | $\sim$3 | | | | |
| 505.1 | 3227 | 8 (2) | $21/2^+ \rightarrow 19/2^+$ | | | $M1$ |
| 506.9 | (4184) | $\sim$1 | $\rightarrow 23/2^+$ | | | |
| 508.3 | 588 | 18 (4) | $7/2^+ \rightarrow 3/2^+$ | 0.96 (20) | | $E2$ |
| 514.8 | 2722 | 28 (4) | $19/2^+ \rightarrow 17/2^+$ | 0.47 (8) | -0.04 (1) | $M1$ |
| 516.3 | 5413 | 8 (2) | $31/2^- \rightarrow 29/2^+$ | 0.57 (12) | | $E1$ |
| 522.2 | 5426 | $\sim$1 | $(29/2)^+ \rightarrow (27/2)^+$ | | | ($M1$) |
| 523.1 | 4993 | 5 (1) | $29/2^+ \rightarrow 27/2^+$ | | | $M1$ |
| 525.1 | 5718 | 18 (4) | $31/2^+ \rightarrow 29/2^+$ | 0.60 (16) | -0.04 (1) | $M1$ |
| 526.9 | 3327 | 50 (5) | $21/2^- \rightarrow 17/2^-$ | 0.93 (10) | 0.04 (1) | $E2$ |
| 538.1 | 4362 | $\sim$3 | $(25/2)^+ \rightarrow (23/2)^+$ | | | ($M1$) |
| 543.1 | 3183 | 16 (3) | $(19/2)^- \rightarrow 19/2^-$ | 0.95 (18) | | ($M1$) |
| 555.0 | 1892 | 654 (33) | $15/2^- \rightarrow 11/2^-$ | 1.06 (12) | 0.06 (1) | $E2$ |
| 563.9 | 2627 | $\sim$3 | $17/2^+ \rightarrow 15/2^+$ | | | $M1$ |
| 564.4 | 4993 | 6 (1) | $29/2^+ \rightarrow 25/2^+$ | | | $E2$ |
| 573.1 | 2780 (L2) | 16 (3) | $(19/2)^+ \rightarrow 17/2^+$ | 0.60 (10) | | ($M1$) |
| 574.2 | (4470) | $\sim$3 | $\rightarrow 25/2^+$ | | | |
| 579.2 | 4204 | 9 (2) | $23/2^+ \rightarrow 23/2^+$ | | | |
| 584.8 | 2792 (L2) | 6 (1) | $\rightarrow 17/2^+$ | | | |
| 587.3 | 6766 | 12 (2) | $35/2^- \rightarrow 33/2^-$ | | | $M1$ |
| 587.9 | 588 | 62 (6) | $7/2^+ \rightarrow 5/2^+$ | | | $M1$ |
| 595.1 | 3279 (L2) | 5 (1) | | | | |
| 597.1 | 6315 | 12 (2) | $33/2^+ \rightarrow 31/2^+$ | 0.49 (10) | | $M1$ |
| 598.9 | 1266 | 48 (6) | $11/2^+ \rightarrow 9/2^+$ | 0.48 (8) | -0.05 (1) | $M1$ |
| 600.1 | 5936 (L2) | $\sim$3 | | | | |
| 603.0 | 3203 (L2) | 4 (1) | $\rightarrow (19/2)^+$ | | | |
| 603.1 | 5073 | 5 (1) | $(29/2)^+ \rightarrow 27/2^+$ | | | ($M1$) |
| 605.1 | 3327 | 34 (5) | $21/2^- \rightarrow 19/2^+$ | 0.53 (10) | 0.06 (2) | $E1$ |
| 611.4 | 3403 (L2) | 4 (1) | | | | |
| 616.8 | 4429 | 6 (1) | $25/2^+ \rightarrow 25/2^+$ | | | |
| 616.9 | 3800 | 26 (5) | $23/2^- \rightarrow (19/2)^-$ | | | ($E2$) |
| 618.0 | 3183 | 11 (2) | $(19/2)^- \rightarrow (15/2)^-$ | | | ($E2$) |
| 621.2 | 2513 | 24 (4) | $15/2^- \rightarrow 15/2^-$ | 1.04 (17) | -0.09 (2) | $M1$ |
| 629.8 | 5780 | 16 (3) | $31/2^- \rightarrow 29/2^-$ | 0.55 (10) | | $M1$ |

**TABLE I –(continued)**

| $E_\gamma$(keV) | $E_{i(f)}$(keV) | Intensity | Spin assignment ($I_i^\pi \rightarrow I_f^\pi$) | DCO | IPDCO | Multipolarity assignment |
|---|---|---|---|---|---|---|
| 630.0 | 4442 | 14 (3) | $27/2^- \rightarrow 25/2^+$ | 0.67 (15) | | $E1$ |
| 630.1 | 4814 | ∼3 | $27/2^+ \rightarrow 23/2^+$ | | | $E2$ |
| 630.4 | 3270 | ∼2 | $\rightarrow 19/2^-$ | | | |
| 642.2 | 4442 | 12 (2) | $27/2^- \rightarrow 23/2^-$ | 1.05 (20) | | $E2$ |
| 656.8 | 4562 (L1) | ∼2 | $\rightarrow (23/2)^+$ | | | |
| 657.2 | 2864 | 316 (16) | $21/2^+ \rightarrow 17/2^+$ | 0.92 (7) | 0.05 (1) | $E2$ |
| 658.1 | 4470 | 28 (4) | $27/2^+ \rightarrow 25/2^+$ | 0.66 (10) | -0.07 (2) | $M1$ |
| 660.1 | 2063 | 20 (3) | $15/2^+ \rightarrow 13/2^+$ | 0.67 (12) | -0.04 (1) | $M1$ |
| 664.6 | 5193 | 38 (5) | $29/2^+ \rightarrow 27/2^+$ | 0.54 (8) | -0.07 (2) | $M1$ |
| 666.8 | 3531 | 65 (7) | $23/2^- \rightarrow 21/2^+$ | 0.59 (10) | 0.05 (1) | $E1$ |
| 667.0 | 667 | 1000 (50) | $9/2^+ \rightarrow 5/2^+$ | | | $E2$ |
| 669.5 | 1337 | 604 (30) | $11/2^- \rightarrow 9/2^+$ | 0.47 (5) | 0.06 (1) | $E1$ |
| 673.2 | 2565 | 18 (4) | $(15/2)^- \rightarrow 15/2^-$ | | | |
| 677.2 | 5413 | 27 (4) | $31/2^- \rightarrow 27/2^-$ | 1.01 (18) | 0.10 (2) | $E2$ |
| 677.7 | 1266 | 98 (7) | $11/2^+ \rightarrow 7/2^+$ | 0.96 (8) | 0.05 (1) | $E2$ |
| 678.0 | 939 | 378 (19) | $11/2^+ \rightarrow 7/2^+$ | 0.87 (7) | 0.06 (1) | $E2$ |
| 686.9 | 3327 | 61 (6) | $21/2^- \rightarrow 19/2^-$ | 0.63 (10) | -0.07 (2) | $M1$ |
| 687.2 | 4814 | 5 (1) | $27/2^+ \rightarrow 23/2^+$ | | | $E2$ |
| 696.3 | (1892) | 8 (2) | $\rightarrow 15/2^-$ | | | |
| 697.8 | 5226 | 10 (2) | $\rightarrow 27/2^+$ | | | |
| 703.6 | 5146 | ∼3 | $\rightarrow 27/2^-$ | | | |
| 707.4 | 3625 | 9 (2) | $23/2^+ \rightarrow 19/2^+$ | | | $E2$ |
| 708.3 | 5150 | 6 (1) | $29/2^- \rightarrow 27/2^-$ | | | $M1$ |
| 711.3 | 2918 | 15 (3) | $19/2^+ \rightarrow 17/2^+$ | 0.62 (12) | | $M1$ |
| 713.9 | 4898 | 5 (1) | $(27/2)^+ \rightarrow 23/2^+$ | | | $(E2)$ |
| 714.8 | 5185 | ∼2 | $(29/2)^+ \rightarrow 27/2^+$ | | | $(M1)$ |
| 715.9 | 4528 | 38 (5) | $27/2^+ \rightarrow 25/2^+$ | 0.54 (10) | -0.04 (1) | $M1$ |
| 722.8 | 5193 | 5 (1) | $29/2^+ \rightarrow 27/2^+$ | | | $M1$ |
| 735.2 | 2627 | 26 (4) | $17/2^- \rightarrow 15/2^-$ | 0.68 (12) | -0.07 (2) | $M1$ |
| 735.7 | 1403 | 464 (23) | $13/2^+ \rightarrow 9/2^+$ | 1.06 (11) | 0.09 (2) | $E2$ |
| 748.2 | 2640 | 569 (28) | $19/2^- \rightarrow 15/2^-$ | 1.02 (10) | 0.06 (1) | $E2$ |
| 785.9 | 2849 | ∼3 | $19/2^+ \rightarrow 15/2^+$ | | | $E2$ |
| 796.8 | 2063 | 77 (7) | $15/2^+ \rightarrow 11/2^+$ | 1.04 (13) | 0.05 (1) | $E2$ |
| 798.2 | 2615 | ∼2 | $\rightarrow 15/2^+$ | | | |
| 804.1 | 2207 | 425 (21) | $17/2^+ \rightarrow 13/2^+$ | 1.00 (8) | 0.10 (2) | $E2$ |
| 820.7 | 5718 | 9 (2) | $31/2^+ \rightarrow 29/2^+$ | 0.67 (15) | | $M1$ |
| 842.9 | 4748 (L1) | ∼1 | $\rightarrow (23/2)^+$ | | | |
| 855.1 | 2918 | 16 (3) | $19/2^+ \rightarrow 15/2^+$ | 0.91 (18) | | $E2$ |
| 876.3 | 6212 (L2) | 4 (1) | | | | |
| 878.0 | 1817 | 228 (16) | $15/2^+ \rightarrow 11/2^+$ | 1.04 (10) | 0.09 (2) | $E2$ |
| 887.3 | 2290 | 25 (4) | $17/2^+ \rightarrow 13/2^+$ | 1.03 (19) | 0.05 (2) | $E2$ |
| 887.8 | 5718 | ∼3 | $31/2^+ \rightarrow (27/2)^+$ | | | $(E2)$ |
| 888.0 | 4109 (L2) | 12 (3) | | | | |
| 891.3 | 3531 | 450 (23) | $23/2^- \rightarrow 19/2^-$ | 1.05 (8) | 0.05 (1) | $E2$ |
| 899.2 | 3106 | 11 (2) | $19/2^+ \rightarrow 17/2^+$ | 0.58 (12) | | $M1$ |
| 902.9 | 5150 | 48 (6) | $29/2^- \rightarrow 25/2^-$ | 0.99 (15) | 0.09 (2) | $E2$ |
| 903.1 | 4528 | 36 (5) | $27/2^+ \rightarrow 23/2^+$ | | | $E2$ |
| 903.3 | 3625 | 91 (12) | $23/2^+ \rightarrow 19/2^+$ | | | $E2$ |
| 903.4 | 3006 (L3) | ∼2 | $\rightarrow (13/2)^+$ | | | |
| 904.7 | 2722 | 125 (10) | $19/2^+ \rightarrow 15/2^+$ | | | $E2$ |
| 908.4 | 2800 | 54 (5) | $17/2^- \rightarrow 15/2^-$ | 0.67 (9) | -0.11 (2) | $M1$ |
| 911.2 | 4442 | 306 (15) | $27/2^- \rightarrow 23/2^-$ | 0.94 (8) | 0.08 (1) | $E2$ |
| 911.9 | 7227 | 8 (2) | $(35/2)^+ \rightarrow 33/2^+$ | | | $(M1)$ |
| 920.4 | 4247 | 61 (6) | $25/2^- \rightarrow 21/2^-$ | 1.03 (16) | 0.07 (2) | $E2$ |
| 930.1 | 3794 (L1) | 4 (1) | $\rightarrow 21/2^+$ | | | |
| 935.8 | 3800 | 7 (1) | $23/2^- \rightarrow 21/2^+$ | | | $E1$ |
| 936.3 | 4736 | 48 (6) | $27/2^- \rightarrow 23/2^-$ | 0.91 (14) | 0.11 (2) | $E2$ |
| 936.7 | 3227 | 22 (4) | $21/2^+ \rightarrow 17/2^+$ | 0.93 (18) | 0.10 (2) | $E2$ |
| 947.8 | 3812 | 170 (12) | $25/2^+ \rightarrow 21/2^+$ | 0.99 (11) | 0.08 (1) | $E2$ |

**TABLE I –(continued)**

| $E_\gamma$(keV) | $E_{i(f)}$(keV) | Intensity | Spin assignment ($I_i^\pi \rightarrow I_f^\pi$) | DCO | IPDCO | Multipolarity assignment |
|---|---|---|---|---|---|---|
| 960.1 | 3824 | 9 (2) | $(23/2)^+ \rightarrow 21/2^+$ | | | ($M1$) |
| 964.1 | 5406 | 4 (1) | $\rightarrow 27/2^-$ | | | |
| 968.9 | 4583 | ∼1 | | | | |
| 971.3 | 5413 | 198 (14) | $31/2^- \rightarrow 27/2^-$ | 0.93 (18) | 0.07 (1) | $E2$ |
| 983.3 | 2800 | 21 (3) | $17/2^- \rightarrow 15/2^+$ | 0.49 (9) | 0.09 (2) | $E1$ |
| 986.3 | 6766 | 25 (4) | $35/2^- \rightarrow 31/2^-$ | 0.91 (18) | 0.09 (2) | $E2$ |
| 1013.8 | 3221 (L2) | 16 (3) | $\rightarrow 17/2^+$ | | | |
| 1020.0 | 3227 | 26 (4) | $21/2^+ \rightarrow 17/2^+$ | 0.89 (18) | 0.06 (2) | $E2$ |
| 1028.3 | 5387 (L2) | 4 (1) | $(23/2)^+ \rightarrow (21/2)^+$ | | | ($M1$) |
| 1028.8 | 6179 | 29 (5) | $33/2^- \rightarrow 29/2^-$ | 1.04 (16) | 0.09 (2) | $E2$ |
| 1041.3 | 3905 (L1) | 13 (3) | $(23/2)^+ \rightarrow 21/2^+$ | 0.51 (12) | | ($M1$) |
| 1042.9 | 3106 | 22 (4) | $19/2^+ \rightarrow 15/2^+$ | 1.03 (20) | 0.11 (2) | $E2$ |
| 1043.9 | 5780 | 39 (5) | $31/2^- \rightarrow 27/2^-$ | 0.93 (15) | 0.12 (2) | $E2$ |
| 1050.0 | 3968 | 7 (1) | $(23/2)^+ \rightarrow 19/2^+$ | | | ($E2$) |
| 1067.6 | 5510 | ∼2 | $\rightarrow 27/2^-$ | | | |
| 1071.0 | (4127) | 4 (1) | $\rightarrow 23/2^+$ | | | |
| 1071.1 | 4976 (L1) | ∼3 | $\rightarrow (23/2)^+$ | | | |
| 1074.1 | 6487 | 105 (7) | $35/2^- \rightarrow 31/2^-$ | 0.94 (9) | 0.05 (1) | $E2$ |
| 1080.6 | (4127) | 4 (1) | $\rightarrow 23/2^+$ | | | |
| 1085.3 | 4897 | 45 (5) | $29/2^+ \rightarrow 25/2^+$ | 0.94 (11) | 0.04 (1) | $E2$ |
| 1086.2 | 5195 (L2) | 5 (1) | | | | |
| 1089.1 | 3521 (L2) | 5 (1) | | | | |
| 1091.9 | 4904 | 5 (1) | $(27/2)^+ \rightarrow 25/2^+$ | | | ($M1$) |
| 1098.1 | 4204 | 16 (3) | $23/2^+ \rightarrow 19/2^+$ | 1.05 (20) | | $E2$ |
| 1098.1 | 7864 | 20 (3) | $39/2^- \rightarrow 35/2^-$ | 0.98 (20) | 0.05 (2) | $E2$ |
| 1100.9 | 2918 | 19 (3) | $19/2^+ \rightarrow 15/2^+$ | 0.90 (18) | 0.07 (2) | $E2$ |
| 1103.9 | 3968 | 5 (1) | $(23/2)^+ \rightarrow 21/2^+$ | | | ($M1$) |
| 1113.2 | 3216 (L3) | ∼3 | $\rightarrow (13/2)^+$ | | | |
| 1118.8 | 3011 | 10 (2) | $19/2^- \rightarrow 15/2^-$ | 0.88(20) | | $E2$ |
| 1123.6 | 2063 | 14 (2) | $15/2^+ \rightarrow 11/2^+$ | 0.93(21) | | $E2$ |
| 1126.1 | 7227 | ∼2 | $(35/2)^+ \rightarrow 33/2^+$ | | | ($M1$) |
| 1127.5 | 7615 | 31 (4) | $39/2^- \rightarrow 35/2^-$ | 0.92 (15) | 0.09 (2) | $E2$ |
| 1129.2 | 4164 (L1) | ∼1 | | | | |
| 1159.7 | 5990 | ∼2 | $(31/2)^+ \rightarrow (27/2)^+$ | | | ($E2$) |
| 1159.9 | 3800 | 33 (5) | $23/2^- \rightarrow 19/2^-$ | 0.94 (15) | 0.07 (2) | $E2$ |
| 1163.9 | 2103 (L3) | 12 (2) | $(13/2)^+ \rightarrow 11/2^+$ | 0.49 (10) | | ($M1$) |
| 1180.8 | 4993 | 9 (2) | $29/2^+ \rightarrow 25/2^+$ | | | $E2$ |
| 1189.6 | 5718 | 15 (3) | $31/2^+ \rightarrow 27/2^+$ | 1.05 (18) | | $E2$ |
| 1197.2 | 5009 | ∼3 | $\rightarrow 25/2^+$ | | | |
| 1202.3 | 4429 | 15 (3) | $25/2^+ \rightarrow 21/2^+$ | 0.97 (18) | | $E2$ |
| 1203.2 | 3306 (L3) | ∼2 | $\rightarrow (13/2)^+$ | | | |
| 1204.2 | 6101 | 21 (3) | $33/2^+ \rightarrow 29/2^+$ | 1.02 (19) | 0.09 (2) | $E2$ |
| 1205.0 | 4736 | 18 (3) | $27/2^- \rightarrow 23/2^-$ | 0.97 (20) | | $E2$ |
| 1209.0 | 4127 | 16 (3) | $23/2^+ \rightarrow 19/2^+$ | 0.94 (22) | | $E2$ |
| 1215.1 | 7981 | 23 (4) | $39/2^- \rightarrow 35/2^-$ | 0.97 (22) | | $E2$ |
| 1224.3 | 2627 | 5 (1) | $17/2^+ \rightarrow 13/2^+$ | | | $E2$ |
| 1224.3 | 4530 (L3) | ∼1 | | | | |
| 1227.1 | 5336 (L2) | 8 (2) | | | | |
| 1263.0 | 4127 | ∼3 | $23/2^+ \rightarrow 21/2^+$ | | | $M1$ |
| 1266.0 | 4184 | 9 (2) | $23/2^+ \rightarrow 19/2^+$ | 0.90 (22) | | $E2$ |
| 1288.8 | 3106 | 9 (2) | $19/2^+ \rightarrow 15/2^+$ | 0.89 (25) | | $E2$ |
| 1297.2 | 7398 | 5 (1) | $(37/2)^+ \rightarrow 33/2^+$ | | | ($E2$) |
| 1314.3 | 4530 (L3) | ∼2 | | | | |
| 1326.2 | 5564 (L1) | ∼2 | | | | |
| 1337.8 | 5780 | 11 (2) | $31/2^- \rightarrow 27/2^-$ | 1.05 (25) | | $E2$ |
| 1352.7 | 6766 | 20 (3) | $35/2^- \rightarrow 31/2^-$ | 0.91 (19) | 0.07 (2) | $E2$ |
| 1352.8 | 2292 | ∼3 | $\rightarrow 11/2^+$ | | | |
| 1353.3 | 7532 | 16 (3) | $(37/2)^- \rightarrow 33/2^-$ | 0.94 (19) | | ($E2$) |
| 1356.0 | 5918 (L1) | ∼1 | | | | |

**TABLE I –(continued)**

| $E_\gamma$(keV) | $E_{i(f)}$(keV) | Intensity | Spin assignment ($I_i^\pi \rightarrow I_f^\pi$) | DCO | IPDCO | Multipolarity assignment |
|---|---|---|---|---|---|---|
| 1361.3 | 4362 | ∼3 | $(25/2)^+ \rightarrow (21/2)^+$ | | | (*E*2) |
| 1376.7 | 7864 | 11 (2) | $39/2^- \rightarrow 35/2^-$ | 0.95 (25) | | *E*2 |
| 1381.2 | 5193 | 6 (1) | $29/2^+ \rightarrow 25/2^+$ | | | *E*2 |
| 1404.2 | 9268 | 12 (2) | $(43/2)^- \rightarrow 39/2^-$ | 0.94 (25) | | (*E*2) |
| 1418.1 | 6315 | ∼3 | $33/2^+ \rightarrow 29/2^+$ | | | *E*2 |
| 1421.8 | 9037 | 12 (2) | $43/2^- \rightarrow 39/2^-$ | 0.94 (30) | 0.07 (2) | *E*2 |
| 1437.1 | 6510 | ∼2 | $(33/2)^+ \rightarrow (29/2)^+$ | | | (*E*2) |
| 1482.1 | 4204 | 6 (1) | $23/2^+ \rightarrow 19/2^+$ | | | *E*2 |
| 1493.9 | 8892 | ∼2 | $(41/2)^+ \rightarrow (37/2)^+$ | | | (*E*2) |
| 1509.1 | 7227 | 4 (1) | $(35/2)^+ \rightarrow 31/2^+$ | | | (*E*2) |
| 1578.8 | 4359 (L2) | 6 (1) | $(21/2)^+ \rightarrow (19/2)^+$ | | | (*M*1) |
| 1591.0 | 10628 | ∼10 | $(47/2)^- \rightarrow 43/2^-$ | | | (*E*2) |
| 1612.7 | 6510 | ∼3 | $(33/2)^+ \rightarrow 29/2^+$ | | | (*E*2) |
| 1652.8 | 9268 | ∼2 | $(43/2)^- \rightarrow 39/2^-$ | | | (*E*2) |
| 1756.4 | 4356 (L2) | 4 (1) | $\rightarrow (19/2)^+$ | | | |
| 1836.2 | (4127) | ∼2 | $\rightarrow 23/2^+$ | | | |
| 2080.9 | (4184) | ∼1 | $\rightarrow 23/2^+$ | | | |
| 2094.1 | (4127) | ∼1 | $\rightarrow 23/2^+$ | | | |
| 2211.1 | 3614 | 5 (1) | $\rightarrow 13/2^+$ | | | |
| 2295.8 | (4184) | ∼1 | $\rightarrow (23/2)^+$ | | | |
| 2492.4 | (4127) | ∼2 | $\rightarrow 23/2^+$ | | | |
| 2580.9 | 5361 (L2) | ∼3 | $(23/2)^+ \rightarrow (19/2)^+$ | | | (*E*2) |
| 2606.9 | 5387 (L2) | ∼2 | $(23/2)^+ \rightarrow (19/2)^+$ | | | (*E*2) |

### A. Positive-parity band structures

The previously observed positive-parity band B1 based on the $5/2^+$ ground state [21,22,33,34] has been extended up to $I^\pi = (41/2)^+$ with addition of the 1297- and 1494 keV transitions (Fig. 2). The structure of band B2 above the 4528 keV $27/2^+$ state [22] is extended further to evolve into a coupled structure consisting of the 665-525-597-912 keV dipole cascade along with the 1190- and 1509 keV crossover transitions [Fig. 3 (a)]. The 1190 keV transition reported by Zhou *et al.* [21] was replaced by the 665-525 keV cascade by Sugawara *et al.* [22]. In the present work, the 1190 keV transition is confirmed to be crossover of the 665-525 keV dipole cascade [Fig. 3 (a)]. New interband $\Delta I = 2$ transitions are observed from various states of band B2 to the corresponding states of band B1 in addition to the earlier observed $\Delta I = 1$ interband transitions [22]. The $23/2^+$ state is the only exception that does not decay to band B1. The 368 keV transition decay reported by Sugawara *et al.* [22] from the 4897 keV $29/2^+$ state in band B1 to the 4528 keV $27/2^+$ state of band B2 could not be confirmed in the present double gate ($\gamma-\gamma-\gamma$) analysis [inset of Fig. 3 (a)]. The 368 keV transition results in a new state at 4896 keV. It is mentioned that the coincident 370-, 902-, and 1204 keV transitions present in the level scheme of $^{102}$Pd have energies close-lying to those supporting the earlier placement of the 368 keV transition [22] in $^{101}$Pd through coincidence relationships.

New level structures labeled L1, L2, and L3 (Fig. 2) are built on the 2864 keV $21/2^+$ state (band B1), 2207 keV $17/2^+$ state (band B1), and 939 keV $11/2^+$ state (band B2), respectively. New states at 2103 keV (structure L3), 2600 keV (structure L2), 2780 keV (structure L2), 3905 keV (structure L1), and 4470 keV decay only through the single transitions of 1164-, 393-, 573-, 1041-, and 658 keV, respectively, to the $11/2^+$ state of band B2, and the $17/2^+$, $17/2^+$, $21/2^+$, and $25/2^+$ states of band B1, respectively. Further, these new states are populated by a number of transitions. The 2600 keV $(19/2)^+$ (structure L1) and 4470 keV $27/2^+$ states lie just below the yrast states of same spin-parity in bands B1 and B2, therefore, these states are possible energetically favored states.

The earlier observed band B6 [22] is extended to $23/2^+$ with the addition of new 1043- and 1098 keV transitions (Fig. 4). The reported 892 keV transition [22] feeding the 2063 keV $15/2^+$ state is not observed. The $15/2^+$, $19/2^+$, and $23/2^+$ states of band B6 decay to the states of band B2 via the new $\Delta I = 0$ and $\Delta I = 2$ transitions [Fig. 3 (d)]. Also, the $15/2^+$ and $19/2^+$ states of band B6 decay to the states of band B1 via new $\Delta I = 1$ transitions. A new 137 keV dipole transition is observed from the $13/2^+$ state of band B1 to the $11/2^+$ state of band B6.

The states involving new sequences of E2 transitions, 937-1202-564 keV and 1209-687 keV [Fig. 3 (d)], are likely to constitute signature partner bands labeled 'a'and 'b'of band B7. The interlinking 179 keV ($29/2^+ \rightarrow 27/2^+$) and 385 keV ($27/2^+ \rightarrow 25/2^+$) transitions are observed. The 1209-687 keV transition cascade in band B7(b) is paralleled by the 1266-630 keV cascade resulting in a new intermediate state at 4184 keV with $I^\pi = 23/2^+$. This state decays to the $25/2^+$ state of band B1 via the 372 keV transition. The 4127 keV $23/2^+$ state of band B7(b) and the 4184 keV $23/2^+$ state are populated by the 1071-, 1081-, 1836-, 2094-, and 2492 keV transitions, and the

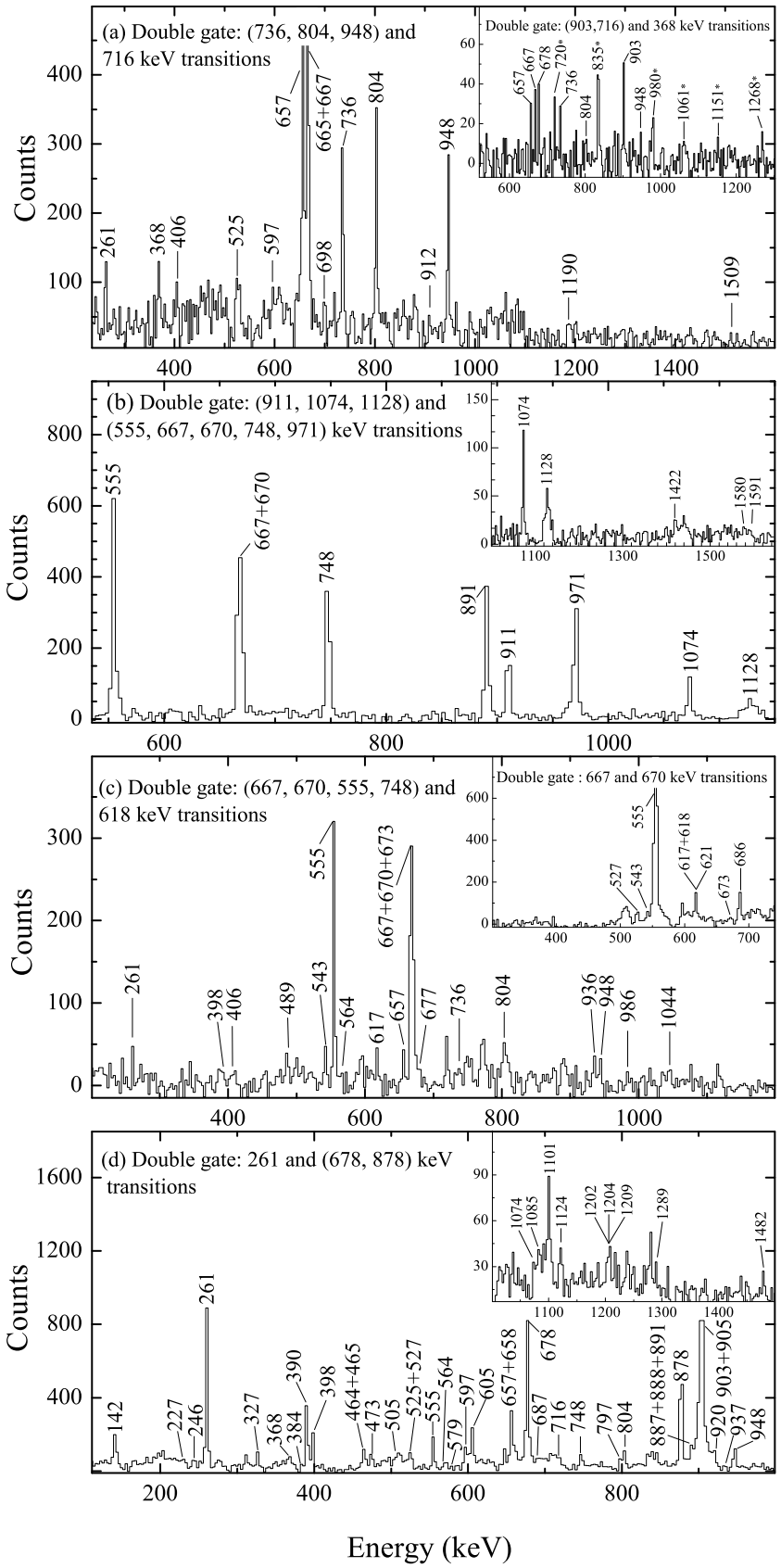


FIG. 3. The double-gated $\gamma$ ray coincidence spectra in $^{101}$Pd generated with coincidence gates on $\gamma$ rays as labeled. Unlabeled insets show the high energy part of the respective labeled main spectra. The spectra depict (a) transitions in dipole strucutre in upper part of band B2, (b) transitions in band B3, (c) transitions in the extended lower spin part of band B5, and (d) transitions in bands B2, B6, and B7. The spectrum shown as inset in (a) infers that the 368 keV transition has no link with upper part of band B1 that is inconsistent with placement by Sugawara *et al.* [22]. The peaks marked (*) correspond to contamination from other nuclei.

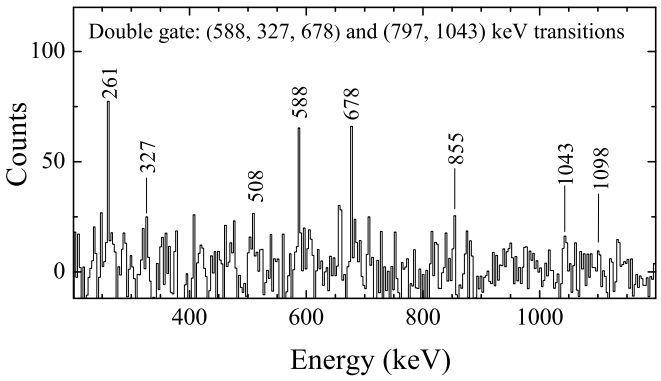


FIG. 4. The double-gated $\gamma$ ray coincidence spectra showing transitions of the positive-parity band B6.

186-, 507-, 2081-, and 2096 keV transitions, respectively, in addition to the transitions shown in Fig. 2.

### B. Negative-parity band structures

The previously reported negative-parity bands B3, B4, and B5 [21,22,33,34] are confirmed up to $43/2^-$, $33/2^-$, and $39/2^-$ states, respectively. The lowest excited negative-parity band B3 based on the $I^\pi = 11/2^-$ state is comprised of electric quadrupole (E2) transitions. The present double gated analysis using $E_\gamma$-$E_\gamma$-$E_\gamma$ cube rules out the 1033- and 1494 keV transitions above the $43/2^-$ reported by Sugawara *et al.* [22] to be part of band B3 (Fig. 2). Sugawara *et al.* [22] have placed the 1423-, 1033-, and 1494 keV transitions in a cascade above the $39/2^-$ state quoting reasons other than the $\gamma$-$\gamma$ coincidence [22]. A spectrum obtained by adding various clean double gated spectra in the $\nu h_{11/2}$ band is shown in Fig. 3 (b). It is worth noting that the excited states in the $^{100}$Pd isotope [8,35] are also populated in the present experiment and a number of coincident transitions in this nucleus have energies close-lying to those in the $\nu h_{11/2}$ band in $^{101}$Pd (Fig. 2). Doppler energy smearing of the $\gamma$ ray peaks further increases their overlapping. Sugawara *et al.* [22] established the level scheme from the single $\gamma$ ray gated coincidence analysis using the $E_\gamma$-$E_\gamma$ matrices. The 1033 keV transition placed by Sugawara *et al.* [22] could be the 1035 keV transition ($15^- \rightarrow 13^-$) of $^{100}$Pd [8,35] populated in their experiment (Fig. 1 and 2 of [22]). The 1035 keV peak is also frequently observed even in the present double gated spectra of transitions in the $\nu h_{11/2}$ band due to close lying transition energies. Multifurcation at the higher spin states and Doppler energy smearing of the $\gamma$ ray peaks constraint further placement of transitions in the $\nu h_{11/2}$ band. Some of the likely candidates identified in the multifurcation are the 1580 keV and 1591 keV transitions above the $39/2^-$ and $43/2^-$ states, respectively. The excited states of band B3 with $11/2 \leq I \leq 31/2$ decay to the states of band B1 via the 489-, 433-, 667-, 630-, 516 keV E1 transitions. The similar E1 transition decay is also observed in $^{99}$Pd and is interpreted as octupole correlations [7].

Excited negative-parity bands B4 and B5 comprise of the E2 transitions and the interlinking M1 transitions, and are extended to higher spin states with addition of the 1353 keV and 1404 keV transitions, respectively. New interlinking 414 keV ($29/2^- \rightarrow 27/2^-$) and 587 keV ($35/3^- \rightarrow 33/2^-$) M1 transitions are also observed. A new 708 keV transition is observed from the $29/2^-$ state of band B4 to the $27/2^-$ state of band B3. A new 1215 keV transition is observed to feed the 6766 keV state of band B5. The DCO and IPDCO ratios for the earlier reported interband 489-, 433-, 667-, and 630 keV transitions, and a new 516 keV interband transition ($31/2^- \rightarrow 29/2^+$) between bands B3 and B1 support their electric dipole character. The present measured DCO and IPDCO ratios support the placement of the 398 keV transition as $11/2^- \rightarrow 11/2^+$. Various level structures have been observed to feed the states of band B3, which are shown in Fig. 2. In addition to the earlier reported 1160 keV transition decay from the lowest $23/2^-$ state of band B5, new decays via the 617-543 keV, and the 617-618-673 keV transition cascades are established to the $19/2^-$ and $15/2^-$ states, respectively, of band B3 [Fig. 3 (c)]. A new 936 keV transition is also observed from the $23/2^-$ state of band B5 to the $21/2^+$ state of band B1. The earlier reported decay from the states of band B5 to those of band B3 [22] via E2 transitions is extended with the addition of the 1377 keV ($39/2^- \rightarrow 35/2^-$) and 1653 keV ( $(43/2)^- \rightarrow 39/2^-$) transitions.

## IV. DISCUSSION

For odd-A nuclei in the near shell-closure mass region, low excitation bands are relatively easier to identify because of the limited possible shell-model configurations. In case of $^{101}$Pd (Z = 46, N = 55), the neutron and proton Fermi surface lie close to the $\nu d_{5/2}$ [431]1/2 and $\nu g_{7/2}$ [420]1/2, and $\pi g_{9/2}$ [422]5/2 Nilsson orbitals, respectively. The level scheme at lower angular momentum consists of bands B1 and B2 which are based on single particle $\nu d_{5/2}$ and $\nu g_{7/2}$ orbitals. The previously observed band B3 built on the $11/2^-$ state at 1337 keV is identified to be based on $\nu h_{11/2}$ orbital [21,22]. The excitation energy *vs* spin plots for the positive-parity and negative-parity bands are shown in Figs. 5 (a) and (b), respectively. The bands B1 and B2 exhibit similar trends. The excitation energy plot of band B6 lies $\sim$ 300 keV above and parallel to those of bands B1 and B2, and exhibits significant deviations at higher spins. To investigate the particle-core reltationship in $^{101}$Pd, the excitation energy plot for the positive-parity yrast band in the core $^{100}$Pd nucleus is also plotted alongwith the negative-parity bands B3, B4, and B5 in $^{101}$Pd [Fig. 5 (b)]. The excitation energy plot as well as $\gamma$ ray energies for band B3 closely follow that for the yrast band in $^{100}$Pd up to $31/2\hbar$, which implies that $\nu h_{11/2}$ is a decoupled participant.

The rotational properties of the observed band structures were investigated by transforming the experimental level energies and spin values into the rotating frame of reference following the prescription of Bengtsson and Frauendorf [36]. The Harris parameters $J_0 = 8.9\ \hbar^2 MeV^{-1}$ and $J_1 = 15.7\ \hbar^4 MeV^{-3}$ [37] were used for this purpose. The alignment ($i_x$)

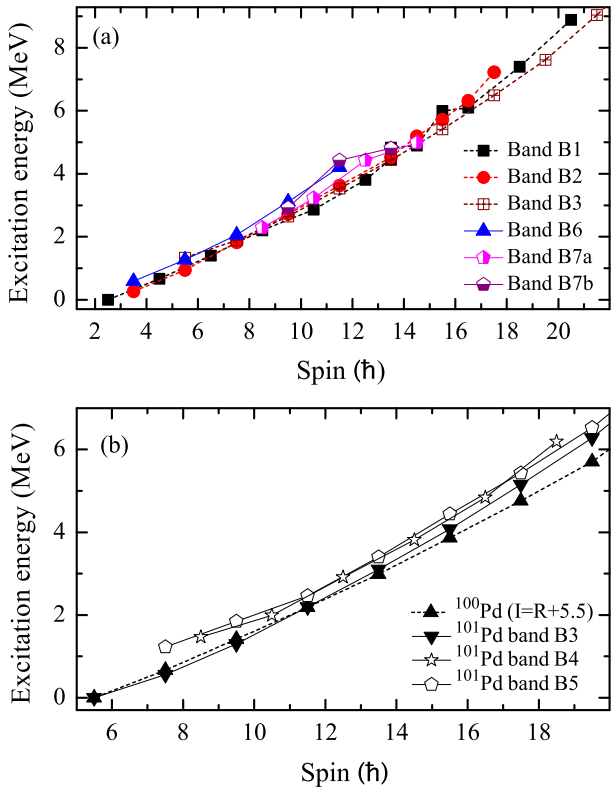


FIG. 5. (Color online) Experimental excitation energy *vs* spin plots for (a) the positive-parity bands B1, B2, B6, and B7 and (b) the negative-parity bands B3, B4, and B5 in $^{101}$Pd. The excitation plot for the g.s. band in $^{100}$Pd [8,35] is compared with that of the $\nu h_{11/2}$ band (B3) in $^{101}$Pd in (b). The spin values for the g.s. band are shifted by 5.5 $\hbar$ and the excitation energy for the $11/2^-$ bandhead state in $\nu h_{11/2}$ band (B3) is shifted to zero.

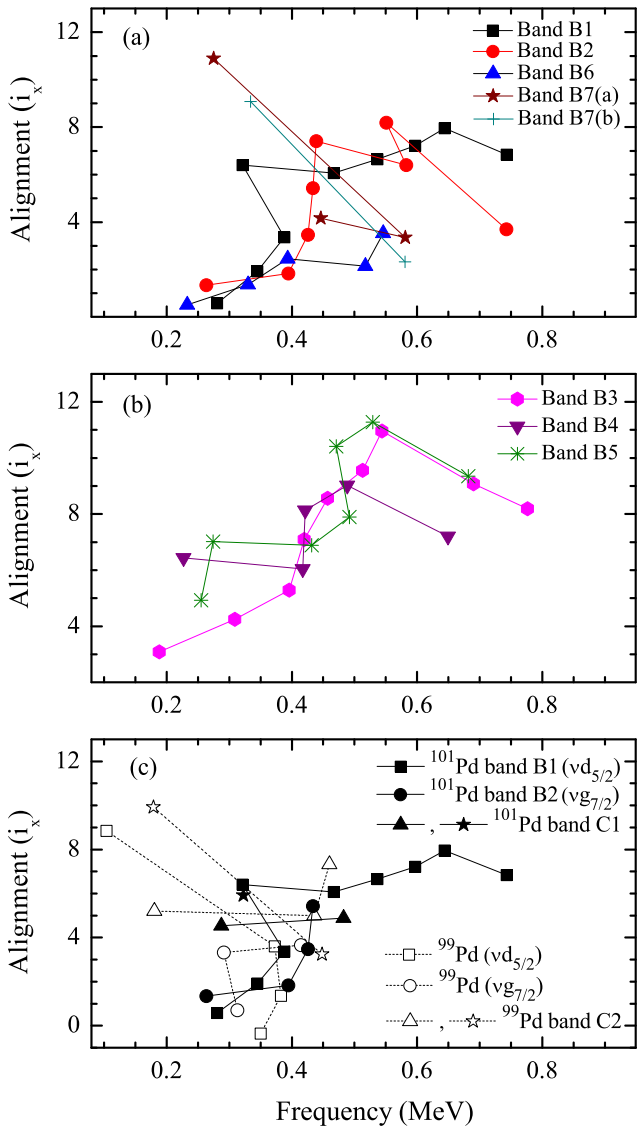


FIG. 6. (Color online) Experimental alignment ($i_x$) plots for (a) the positive-parity bands B1, B2, B6, and B7, and (b) the negative-parity bands B3, B4, and B5 in $^{101}$Pd, and (c) the $\nu d_{5/2}$ and $\nu g_{7/2}$ bands in odd-A $^{99,101}$Pd isotopes [7]. Bands C1 and C2 in (c) correspond to the positive-parity high spin coupled part in the $^{101}$Pd (band B2) and $^{99}$Pd [7], respectively.

and Routhian ($e'$) plots for the bands B1-B7 are shown in Figs. 6 and 7, respectively.

### A. Positive-parity bands

The positive-parity bands B1 and B2 are based on the $5/2^+$ ground state and the $7/2^+$ 261 keV excited state, respectively [21,22,33]. It is noted that bands B1 and B2 are assigned the $\nu d_{5/2}$ and $\nu g_{7/2}$ configurations [21,22], respectively. Several interband transitions between bands B1 and B2 indicate admixture of the assigned single particle configurations. This is a prevalent feature in this mass region.

The first bandcrossing in band B1 is observed at $\hbar\omega \sim 0.36$ MeV, which is lower than that observed for band B2 at $\hbar\omega \sim 0.43$ MeV [Fig. 7 (a)]. The observed alignment gain in bands B1 and B2 are high, $\Delta i_x \sim 6\ \hbar$, [Fig. 6 (a)] which along with the blocking arguments favor alignment of the $\pi g_{9/2}$ pair. The alignment plot for the coupled level strucutre in the upper portion of the $\nu g_{7/2}$ band in $^{99}$Pd [7] exhibit close similarity with that observed for the high spin coupled part of band B2 above the $27/2^+$ level [Fig. 6 (c)].

Routhian plot of band B6 lies parallel to that of single quasiparticle band B1 ($\nu d_{5/2}$) and band B2 ($\nu g_{7/2}$). It exhibits small initial alignment, $i_x \sim 2\ \hbar$, with indication of upbend at $\hbar\omega \sim 0.5$ MeV [Fig. 6 (a)]. These features infer that band B6 is also based on single quasiparticle $\nu d_{5/2}/\nu g_{7/2}$ configuration, however, with different K value.

The states in band B7(a) decay by the $\Delta$I = 0, 2 transitions to respective states in band B1, and $\Delta$I = 1 transitions to re-

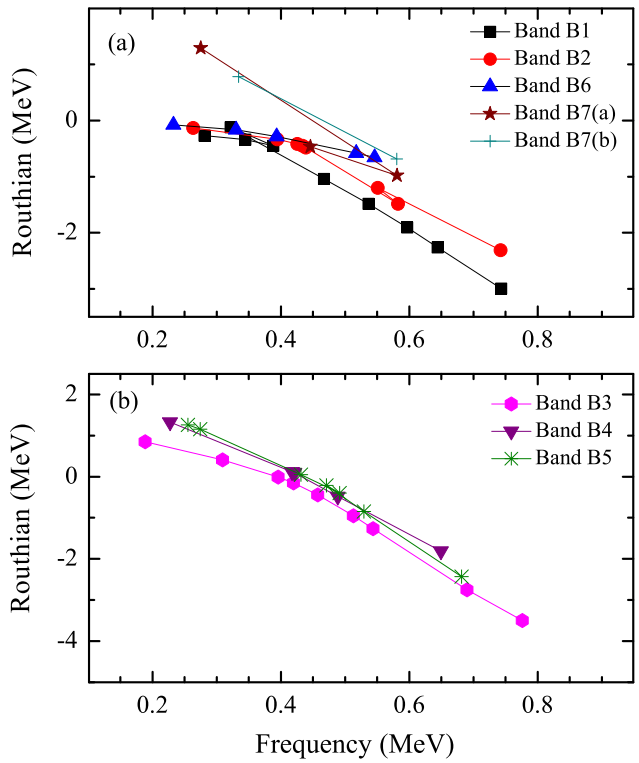


FIG. 7. (Color online) Experimental Rouhtian ($e'$) plots for (a) the positive-parity bands B1, B2, B6, and B7, and (b) the negative-parity bands B3, B4, and B5 in $^{101}$Pd.

spective states in band B2. The states in band B7(b) decay by the ΔI = 1 transitions to respective states in band B1, and ΔI = 2 transitions to respective states in band B2. The $17/2^+$ and $19/2^+$ states also decay via the ΔI = 1 and ΔI = 2 transitions, respectively, to the respective states in band B6. Interestingly, the $23/2^+$ state of band B2 decays to the $19/2^+$ state of band B7(b) via the 707 keV transition and does not decay to any of the states of band B1. Relatively large initial alignment, $i_x \sim 4\hbar$, and slope of its Routhian indicate band B7 to be a three quasiparticle band. The decay pattern of band B7 favors it to be based on three quasiparticle $\nu d_{5/2} \otimes \nu g^2_{7/2}$ configuration and the bandhead $17/2^+$ correspond to fully aligned state.

### Projected shell model calculations

Projected shell model (PSM) is an efficient theoretical technique to describe the properties of nuclear states in medium and heavy mass nuclei. PSM uses deformed single particle basis states and incorporates pairing correlation using BCS calculations. In order to calculate the observable quantities, the spherical shell model is diagonalized in the angular momentum projected deformed basis. For the odd-neutron systems, the PSM basis are composed of one quasiparticle, $a^\dagger_\nu|\Phi>$, and three quasiparticle, $a^\dagger_\nu a^\dagger_{\pi_i} a^\dagger_{\pi_j}|\Phi>$, configurations, where $|\Phi>$ denote the quasiparticle vacuum, $a^\dagger_\nu$ and $a^\dagger_\pi$ are the quasiparticle creation operators, with the index $\nu$ ($\pi$) being the neutron (proton) quantum numbers. The above basis states are projected to good angular momentum states using the standard projection formalism [38–40]. The projected states are then used as the basis states to diagonalize the shell model Hamiltonian.

As in the earlier PSM calculations, we use the quadrupole-quadrupole plus pairing Hamiltonian [41]

$$\hat{H} = \hat{H}_0 - \frac{1}{2}\chi\sum_\mu \hat{Q}^\dagger_\mu \hat{Q}_\mu - G_M\hat{P}^\dagger\hat{P} - G_Q\sum_\mu \hat{P}^\dagger_\mu \hat{P}_\mu. \quad (1)$$

In the above equations, $\hat{H}_0$ is the spherical single-particle Hamiltonian, which contains a proper spin-orbit force. The $QQ$-force strength $\chi$ in Eq. (1) is adjusted such that the physical quadrupole deformation, $\varepsilon_2$, is obtained as a result of the self-consistent mean-field calculations [41]. The monopole pairing strength $G_M$ is of the standard form: $G_M = [20.12 \mp 13.13(N-Z)/A]/A$, with "−" for neutrons and "+" for protons. This choice of $G_M$ is appropriate for the single-particle space employed in the present calculations, where three major oscillator shells are used for each type of nucleon ($N$ = 3, 4, and 5 for neutrons, and $N$= 2, 3, and 4 for protons). The quadrupole pairing strength $G_Q$ is assumed to be proportional to $G_M$ with the proportionality constant being fixed as usual to 0.20 [41]. These interaction strengths, although not exactly the same, are consistent with those used earlier in the PSM calculations [41].

PSM calculations have been performed for $^{101}$Pd by constructing the quasiparticle basis space with axial deformation parameters, $\varepsilon_2 = 0.128$ and $\varepsilon_4 = -0.020$ adopted from the earlier studies [42]. The projected energies obtained for each intrinsic configuration are plotted in Fig. 8. The plots referred to as the band diagram provide an insight into the observed band structures. The lowest band structure is obtained for the intrinsic $\nu d_{5/2}$ state having, $K = 1/2$, which is expected to have large signature splitting. It is noted that the unfavoured states are quite high in energy and for $I = 9/2, 13/2$, and $17/2$, the lowest energy states originate from the projection of one-quasiparticle $\nu g_{7/2}$ state with $K = 9/2$. Further, it is interesting to note that high-K three quasiparticle configurations cross the one quasiparticle configurations at $I = 21/2$. As the yrast configuration is expected to be dominated by $K = 1/2$, which is aligned towards the rotational axis, and that the high-K states become yrast after the bandcrossing, it is interpreted that there is crossing from principal-axis cranking (PAC) to the tilted-axis cranking (TAC). This implies that before $I = 21/2$, E2 transitions should dominate the decay, whereas after the crossing, $M1$ decay should be predominant.

In the band diagram shown in Fig. 8, only the band structures close to the yrast line are depicted. In the actual analysis, the projected band structures are calculated for all the states close to the Fermi surface within a window of $\sim$ 3 MeV. This window results into around 50 intrinsic states from which angular momentum projection is performed. These projected states are then used as the basis states to diagonalize the shell

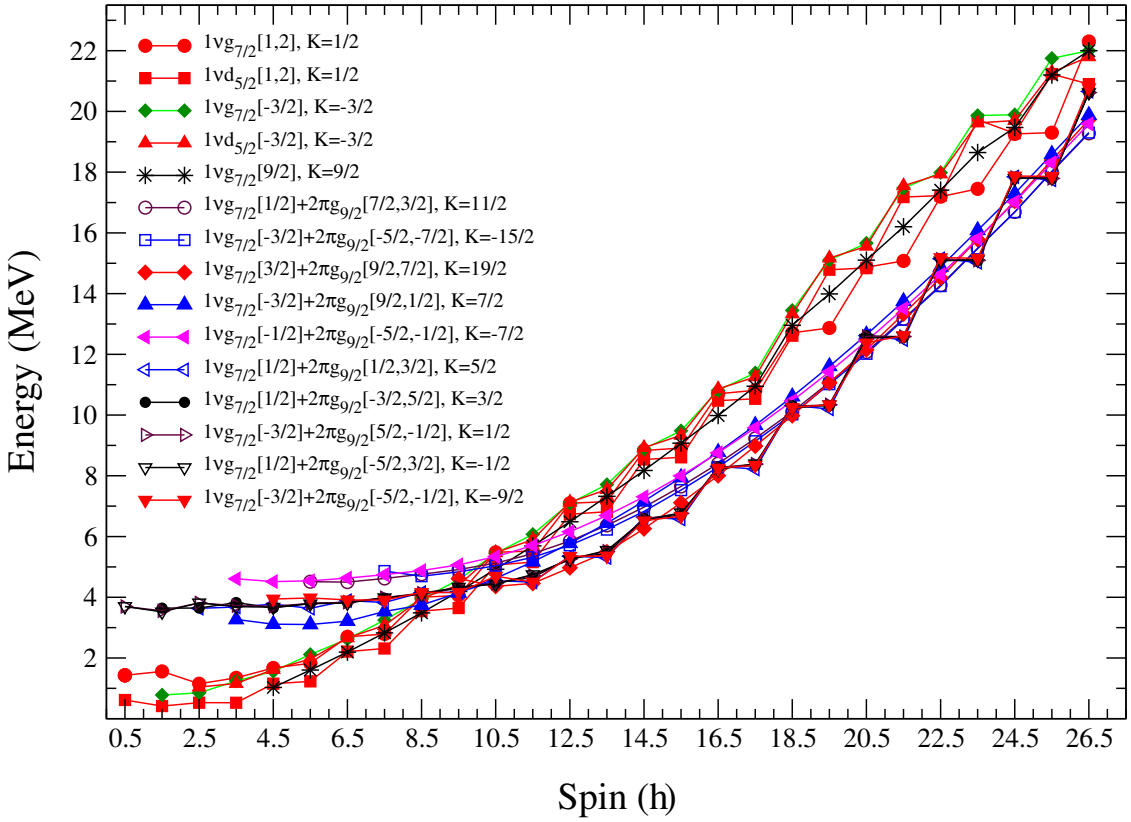


FIG. 8. (Color online) Band diagram for the positive parity bands for $^{101}$Pd depicting the angular-momentum projected bands from one- and three-quasiparticle states. For clarity, only the lowest projected bands are shown and in the numerical calculations, projection has been performed from fifty intrinsic states.

model Hamiltonian. The energies obtained after the diagonalization for the positive parity bands are depicted in Fig. 9 along with the present experimental results. PSM calculated energies in Fig. 9 are separated into various band structures based on the wavefunction analysis. It is evident that bands B1 and B2 up to $I = 23/2$ result from the same intrinsic configuration of $K = 1/2$ and $3/2$, and are actually signature partner states. However, after the bandcrossing, the two bands have very different intrinsic structures and hence, these are labeled as two different bands. Band B1 is dominated by the three quasiparticle state with $K = 19/2$ and whereas band B2 is dominated by $K$ = 9/2 three quasiparticle state.As discussed above, coupled structures are expected due to dominance of high-K configurations after the crossing. Experimental level scheme, indeed, does show a few dipole transitions above the $I = 23/2$ in band B2 (Fig. 9) and also, both the signatures are observed in band B1. More experimental work needs to be performed in order to further probe the predicted transition from PAC to TAC for $^{101}$Pd. It is worth mentioning that similar dipole structure has also been observed at higher spins in the the $\nu g_{7/2}$ band in $^{99}$Pd [7] as discussed earlier in this section. Band B6 has dominant $K$ = 1/2, 3/2, and 9/2 one quasiparticle state before the bandcrossing and after that it has dominant $K = 7/2$ and $19/2$ three quasiparticle configurations. In the present work, band B6 is observed only up to beginning of bandcrossing.

### B. Negative-parity bands

The negative-parity structures in $^{101}$Pd mainly consist of bands B3, B4, and B5. Band B3 based on the $11/2^-$ state at 1337 keV is assigned $\nu h_{11/2}$ configuration [21,22,33]. The lowest excited negative-parity band B3 consisting of $\Delta$I = 2 transitions is built on the favored signature of $\Omega$ = 1/2 orbital of the $\nu h_{11/2}$ subshell [21,22,33]. The unfavored signature band is not expected to be observed in this mass region due to large signature splitting. The first bandcrossing in band B3 is observed at $\hbar\omega \sim 0.41$ MeV followed by the second bandcrossing at $\hbar\omega \sim 0.53$ MeV. Since the $(\nu h_{11/2})^2$ pair alignment is blocked in band B3, the likely candidates generating the observed total alignment gain of $\Delta i_x \sim 7\hbar$ are the $(\nu g_{7/2})^2$ and $(\pi g_{9/2})^2$ pairs. The E1 transitions from various states of the $\nu h_{11/2}$ band to the $\nu d_{5/2}$ band have been observed and the extracted B(E1) values are found to be $\sim 10^{-6}$ W.u. This aspect corresponding to $\nu h_{11/2}$ and $\nu d_{5/2}$ orbitals ($\pi$ = -1, $\Delta l$ = $\Delta j$ = 3) related to possible octupole correlations in the $^{101}$Pd

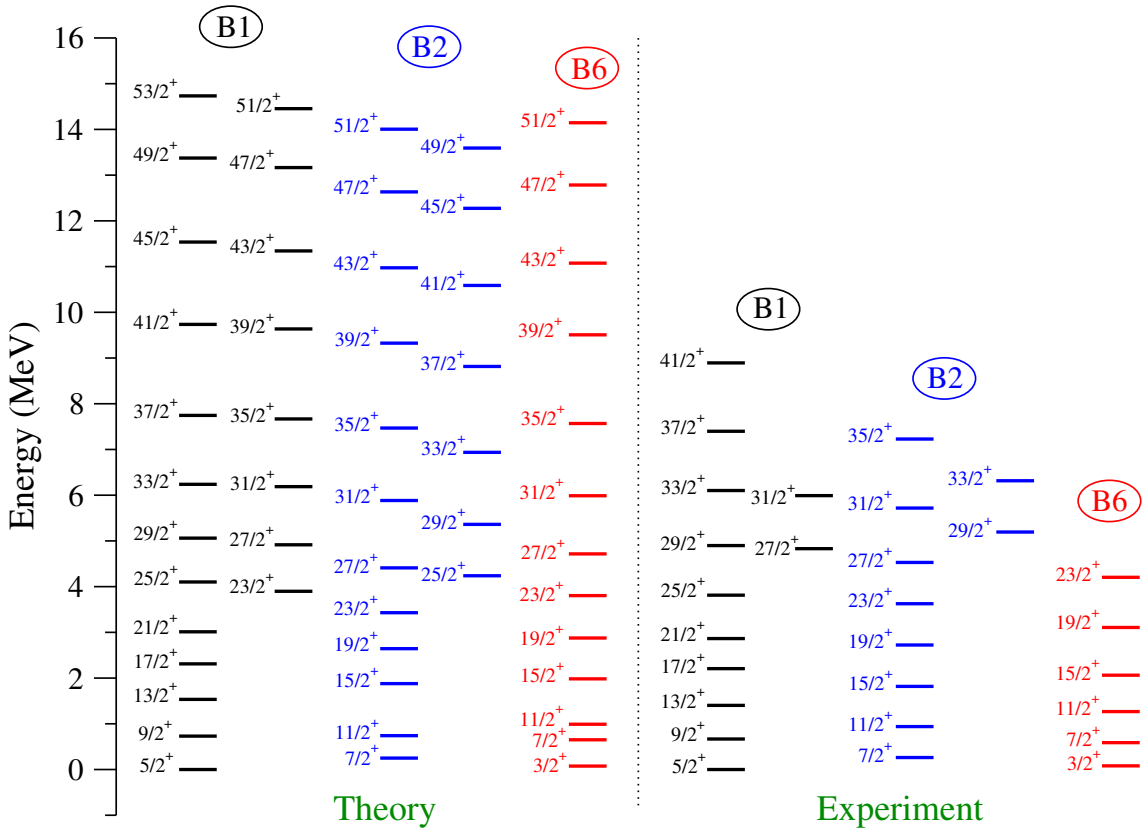


FIG. 9. (Color online) Comparison of the calculated level energies for the positive-parity bands with the present experimental data for $^{101}$Pd.

nucleus has been discussed by Sugawara *et al.* [22]. Octupole correlations have also been reported in the $^{99}$Pd nucleus [7].

Routhians for the excited bands B4 and B5 lie close to each other. At higher spins, the alignment plot of band B5 closely follow that of band B3, and its Routhian is about $\Delta e' \sim 250$ keV above that of band B3. Bands B4 and B5 are coupled through M1 transitions. The B(M1)/B(E2) ratios $\sim 1.5$ $\mu_N(eb)^{-2}$ for various states are deduced in these bands.

### Tilted-axis cranking shell model calculations

The observed negative-parity bands are assigned configurations on the basis of comparison of the rotational properties with those calculated using the tilted-axis cranking (TAC) shell model [43,44]. The basic configuration for these negative parity excited bands are expected to be the prolate-driving $\nu h_{11/2}$ orbital. The hybrid version of TAC model has been used to interpret the observed features of the negative parity bands. Various expected configurations in this mass region, viz., $\nu(h_{11/2})$, $\nu[h_{11/2}(g_{7/2}/d_{5/2})^2]$, and $\pi(g_{9/2})^{-2} \otimes \nu(h_{11/2})$ [21], and $\pi(g_{9/2})^{-4} \otimes \nu(h_{11/2})$, $\pi(g_{9/2})^{-2} \otimes \nu[h_{11/2}(g_{7/2}/d_{5/2})^2]$, $\pi(g_{9/2})^{-4} \otimes \nu[h_{11/2}(g_{7/2}/d_{5/2})^2]$ [22, 23], are considered for the TAC model calculations. The quadrupole deformation parameter ($\varepsilon_2$), the hexadecapole deformation parameter ($\varepsilon_4$), the triaxiality parameter ($\gamma$), and the average tilt-angle ($\theta$) determined corresponding to self-consistent minima for various configurations in $^{101}$Pd are summarized in Table II. In these calculations, the pairing parameters are chosen as 80% of the odd-even mass difference, i.e., $\Delta_\pi = 0.9799$ MeV and $\Delta_\nu = 1.0313$ MeV.

The TAC model calculated spin *vs* frequency plots for the various configurations are shown in Figs. 10 (a) and (b) along with the experimental ones for the negative-parity bands B3, B4, and B5. Keeping in mind that these parameters are sensitive function of the pairing gap parameter, the plot for band B3 at lower spins are in reasonably good agreement with the predicted ones for the $\nu h_{11/2}$ configuration [Fig. 10 (a)]. The TAC model calculations predict the first bandcrossing resulting from alignment of the $\nu(g_{7/2}/d_{5/2})^2$ pair followed by the second bandcrossing arising from the $\pi(g_{9/2})^{-2}$ alignment. The middle portion of band B3 is well reproduced for the $\nu[h_{11/2}(g_{7/2}/d_{5/2})^2]$ configuration and the higher portion is well reproduced for the $\pi(g_{9/2})^{-2} \otimes \nu[h_{11/2}(g_{7/2}/d_{5/2})^2]$ configuration [Fig. 10 (a)]. Similar inferences were obtained from recent calculations by Zhang [24] using the cranked shell model with pairing correlations treated by a particle number conserving method (PNC-CSM). It is added that the deformation values for the configurations assigned on the basis of TAC model calculations decrease successively from $\varepsilon_2 = 0.143$ to $\varepsilon_2 = 0.108$ along band B3 (Table II), which can also contribute to decreasing trend for the B(E2) values along the band.

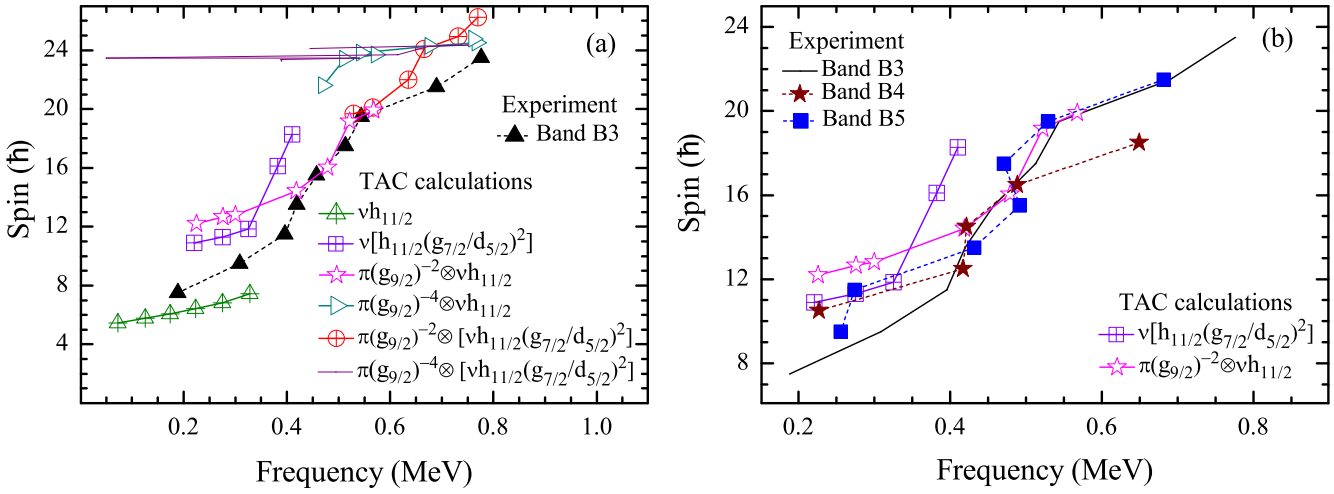


FIG. 10. (Color online) The comparison of experimentally observed spin *vs* frequency plots with the TAC model calculations for various configurations for the negative-parity (a) band B3 and (b) bands B4 and B5 in $^{101}$Pd.

TABLE II. The TAC model parameters calculated for the various configurations in $^{101}$Pd.

| Configuration | $\varepsilon_2$ | $\varepsilon_4$ | $\gamma$ | $\theta$ |
|---|---|---|---|---|
| $\nu(h_{11/2})$ | 0.143 | -0.016 | 11.0° | 85° |
| $\nu[h_{11/2}(d_{5/2}/g_{7/2})^2]$ | 0.128 | -0.013 | 17.4° | 85° |
| $\pi(g_{9/2})^{-2}\otimes\nu[h_{11/2}(d_{5/2}/g_{7/2})^2]$ | 0.108 | -0.017 | 19.5° | 85° |
| $\pi(g_{9/2})^{-2}\otimes\nu(h_{11/2})$ | 0.123 | -0.019 | -11.6° | 85° |
| $\pi(g_{9/2})^{-4}\otimes\nu(h_{11/2})$ | 0.093 | -0.010 | 17.6° | 85° |
| $\pi(g_{9/2})^{-4}\otimes\nu[h_{11/2}(d_{5/2}/g_{7/2})^2]$ | 0.093 | -0.010 | 31.2° | 85° |

The $\pi(g_{9/2})^{-4}\otimes\nu h_{11/2}$ configuration is ruled out for the higher portion of band B3 as the TAC calculated plot lies higher than the observed experimental values [Fig. 10 (a)]. Beyond the alignment of second $\pi(g_{9/2})^{-2}$ pair, the $\pi(g_{9/2})^{-4}\otimes\nu[(h_{11/2}(g_{7/2}/d_{5/2})^2]$ configuration with predicted triaxial shape (Table II) fails to generate angular momentum with further increase in frequency [Fig. 10 (a)], i.e., it does not support band formation. The fully aligned terminating state is not observed in the present experiment.

Further, the DSAM lifetime analysis for various states in band B3 from the present backed-target experiment demonstrates significantly decreasing trend for the B(E2) values in the spin range $31/2\hbar \leq I \leq 43/2\hbar$ [45,46]. These observations are interpreted in the framework of semiclassical particle rotor model (PRM) calculations as antimagnetic rotation (AMR) based on closing of the oppositely aligned $g_{9/2}$ proton holes in the $\pi(g_{9/2})^{-2}\otimes\nu[h_{11/2}(g_{7/2}/d_{5/2})^2]$ double-shears configurations [45]. The aforementioned observations differ significantly from the DSAM based lifetime measurements in band B3 by Sugawara *et al.* [22,23], wherein the decreasing trend in the B(E2) values has been reported in the lower portion in band B3 with $19/2\hbar \leq I \leq 31/2\hbar$ and interpreted as AMR arising due to closing of the shears with the proton blade of each shear consisting of angular momentum vector of two $\pi g_{9/2}$ holes [23,24]. It is unlikely as making symmetric shears out of $(\pi g_{9/2})^{-4}$ has to be very selective and involves strong proton-proton interaction strength. In general, the AMR bands based on the $\pi g_{9/2}^{-2}\otimes\nu[(g_{7/2}/d_{5/2})^m(h_{11/2})^n]$ configurations have been identified in $^{105-108,110}$Cd [17,18] with (m= 0, 1, 2, and n = 1, 2) and $^{104}$Pd [19] with (m = 2 and n = 2) on the basis of lifetime measurements. The present TAC model calculations also infer the $\pi(g_{9/2})^{-2}$ based configuration for band B3.

Bands B4 and B5 exhibit initial alignment $i_x \sim 6\ \hbar$ and bandcrossing at $\hbar\omega \sim 0.42$ and 0.48 MeV, respectively, and with alignment gains $\Delta i_x \sim 3\ \hbar$ and $\sim 5\ \hbar$, respectively [Fig. 6 (b)]. The excited band B5 decays through the stretched E2 transitions to the respective states in band B3. The decaying out E2 transitions are of nearly same energy $\sim$ 1.3 MeV and the B(E2)$_{out}$/B(E2)$_{in}$ ratios for the various states range $\sim$ 0.05-0.20. It infers the structure of band B5 to be similar to the middle portion of the observed band B3. Band B5 is assigned the $\nu[h_{11/2}(g_{7/2}/d_{5/2})^2]$ configuration, which is well reproduced in TAC calculations with predicted prolate shape ($\varepsilon_2$ = 0.128, $\gamma$ = 17.4°) [Fig. 10 (b) and Table II]. The observed portion of band B4 is reproduced by the TAC calculations for the $\pi(g_{9/2})^{-2}\otimes\nu(h_{11/2})$ configuration. Band B5 with the assigned configuration $\nu[h_{11/2}(g_{7/2}/d_{5/2})^2]$ permits rotational alignment of $\pi(g_{9/2})^{-2}$ with a larger alignment gain $\Delta i_x \sim 5\ \hbar$ [Fig. 6 (b)]. Band B4 with the assigned configuration $\pi(g_{9/2})^{-2}\otimes\nu(h_{11/2})$ permits rotational alignment of $\nu(g_{7/2}/d_{5/2})^2$ with a lower alignment gain $\Delta i_x \sim 3\ \hbar$ [Fig. 6 (b)]. The TAC model calculations predict alignment of the

$(g_{9/2})^{-2}$ proton pair and the $(g_{7/2}/d_{5/2})^2$ neutron pair for the $\nu[h_{11/2}(g_{7/2}/d_{5/2})^2]$ and $\pi(g_{9/2})^{-2} \otimes \nu(h_{11/2})$ bands, respectively, at somewhat similar rotational frequencies as observed for the negative-parity bands (Fig. 10 (b)). Interestingly, the TAC calculations predict almost same $\varepsilon_2$ values for the $\pi(g_{9/2})^{-2} \otimes \nu(h_{11/2})$ and $\nu[h_{11/2}(g_{7/2}/d_{5/2})^2]$ configurations assigned to bands B4 and B5, respectively, and differ in triaxiality parameter $\gamma \sim$ -12° and 17° associated with weakly oblate and prolate shapes, respectively.

## V. SUMMARY

The $\gamma$ ray spectroscopic investigation of the $^{101}$Pd nucleus following population through the $^{75}$As($^{31}$P, $2p3n$) reaction at $E_{lab}$ = 125 MeV and the deexcitations has resulted in substantial extension of band structures. The level scheme consisting of seven bands is established up to excitation energy $\sim$ 10.5 MeV and spin $\sim 47/2\hbar$ with the addition of more than 100 new transitions. The observed positive-parity level structures in $^{101}$Pd have been interpreted in the framework of PSM calculations. The positive-parity single quasiparticle bands undergo transition to the high-K three quasiparticle configurations after the bandcrossing. The observed negative-parity level structures have been interpreted in the framework of TAC model calculations. The $\nu h_{11/2}$ negative-parity band is identified to exhibit successive $(\nu g_{7/2})^2$ and $(\pi g_{9/2})^2$ pair alignments. The higher excited negative-parity bands are found to be based on the $\pi(g_{9/2})^{-2} \otimes \nu(h_{11/2})$ and $\nu[h_{11/2}(g_{7/2}/d_{5/2})^2]$ configurations exhibiting weakly oblate and prolate shapes, respectively.

## ACKNOWLEDGMENTS

Authors would like to thank the TIFR-BARC Pelletron Linac Facility staff for providing good quality beam. The help and cooperation of the members of the INGA collaboration for setting up the array are acknowledged. The authors would also like to thank the Department of Science and Technology, Government of India, for providing funding for the INGA project (No. IR/S2/PF-03/2003-I). Financial support from IUAC, New Delhi (Project Nos. IUAC/XIII.7/UFR-50302 and IUAC/XIII.7/UFR-54315), UGC, New Delhi (Project No. 42-809/2013 (SR)), DST, New Delhi (FIST), and U. S. National Science Foundation (Grant No. PHY-1419765) are duly acknowledged. Financial support from UGC, New Delhi, under the Center of Advanced Study Funds, and Basic Scientific Research fellowship in Sciences (for V.S.) are duly acknowledged.

[1] W. Reviol *et al.*, Nucl. Phys. A **557**, 391 (1993).
[2] S. Frauendorf, Rev. Mod. Phys. **73**, 463 (2001).
[3] J. Timár *et al.*, Phys. Rev. C **62**, 044317 (2000).
[4] J. Timár *et al.*, Eur. Phys. J. A **4**, 11 (1999).
[5] J. Gizon *et al.*, Phys. Rev. C **59**, R570 (1998).
[6] J. Cederkäll *et al.*, Z. Phys. A **359**, 227 (1997).
[7] S. Sihotra *et al.*, Phys. Rev. C **83**, 024313 (2011).
[8] G. E. Perez *et al.*, Nucl. Phys. A **686**, 41 (2001).
[9] J. Gizon *et al.*, Phys. Lett. B **410**, 95 (1997).
[10] B. M. Nyakó *et al.*, Phys. Rev. C **60**, 024307 (1999).
[11] J. Cederkäll *et al.*, Eur. Phys. J. A **1**, 7 (1998).
[12] D. Sohler *et al.*, Eur. Phys. J. A **16**, 171 (2003).
[13] S. H. Yao *et al.*, Phys. Rev. C **89**, 014327 (2014).
[14] C. J. Chiara *et al.*, Phys. Rev. C **61**, 034318 (2000).
[15] C. J. Chiara *et al.*, Phys. Rev. C **64**, 054314 (2001).
[16] A. Gadea *et al.*, Phys. Rev. C **55**, R1 (1996).
[17] D. Choudhury *et al.*, Phys. Rev. C **87**, 034304 (2013).
[18] S. Roy *et al.*, Phys. Lett. B **694**, 322 (2011).
[19] N. Rather *et al.*, Phys. Rev. C **89**, 061303(R) (2014).
[20] A. D. Ayangeakaa *et al.*, Phys. Rev. Lett. **110**, 102501 (2013).
[21] H. B. Zhou *et al.*, Eur. Phys. J. A **47**, 107 (2011).
[22] M. Sugawara *et al.*, Phys. Rev. C **86**, 034326 (2012).
[23] M. Sugawara *et al.*, Phys. Rev. C **92**, 024309 (2015).
[24] Z.-H. Zhang, Phys. Rev. C **94**, 034305 (2016).
[25] R. Palit *et al.*, Nucl. Instrum. Methods Phys. Res., Sect. A **680**, 90 (2012).
[26] S. Muralithar *et al.* Nucl. Instrum. Methods Phys. Res., Sect. A **622**, 281 (2010).
[27] S. Kumar *et al.*, J. Phys. G **41**, 105110 (2014).
[28] V. Singh *et al.*, Phys. Rev. C **94**, 044320 (2016).
[29] D. C. Radford, Nucl. Instrum. Methods Phys. Res., Sect. A **361**, 297 (1995); **361**, 306 (1995).
[30] K. Starosta *et al.*, Nucl. Instrum. Methods Phys. Res., Sect. A **423**, 16 (1999).
[31] J. Blachot, Nucl. Data Sheets **83**, 1 (1998).
[32] S . I . Hayakawa, I. R. Hyman, and J. K. P. Lee, Nucl. Phys. A **296**, 251 (1978).
[33] R. Popli, F. A. Rickey, and P. C. Simms, Phys. Rev. C **22**, 1121 (1980).
[34] S. Zhu, Ph.D. thesis, University of Notre Dame (2004) (unpublished).
[35] S. Zhu *et al.*, Phys. Rev. C **64**, 041302(R) (2001).
[36] R. Bengtsson and S. Frauendorf, Nucl. Phys. A **327**, 139 (1979).
[37] S. Kumar *et al.*, Phys. Rev. C **89**, 034303 (2014).
[38] P. Ring and P. Schuck, *The Nuclear Many Body Problem* (Springer-Verlag, New York), (1980).
[39] K. Hara and S. Iwasaki, Nucl. Phys. A **332**, 61 (1979).
[40] K. Hara and S. Iwasaki, Nucl. Phys. A **348**, 200 (1980).
[41] K. Hara and Y. Sun, Int. J. Mod. Phys. E **4**, 637 (1995).
[42] P. Moller, J. R. Nix, W. D. Myers, and W. J. Swiatecki, At. Data Nucl. Data Tables **59**, 185 (1995).
[43] V. I. Dimitrov, F. Dönau, and S. Frauendorf, Phys. Rev. C **62**, 024315 (2000).
[44] S. Frauendorf and J. Meng, Nucl. Phys. A **617**, 131 (1997).
[45] V. Singh *et al.* (To be published).
[46] V. Singh *et al.*, Proc. DAE-BRNS Symp. Nucl. Phys. **59**, 224 (2014); **60**, 180 (2015).